

Validation of a Model for Open Rotor Noise Predictions and Calculation of Shielding Effects using a Fast BEM

Markus Lummer^{*}, Christoph Richter[†], Carsten Prüber[‡], Jan Delfs[‡]

For application in BEM/FMM shielding calculations a simple analytical model for the loading noise of contra rotating open rotors (CRORs) with different rotational speeds is derived. Following previous work of S.L.A. Glegg, the model is formulated in frequency domain and the pressure is approximated by a set of dipoles on circles on the propeller disk. The dipole strength depends on the blade loading function and can be obtained, e.g., by CFD calculations. For arbitrary rotational speeds, the blade loading function is not a periodic function on the propeller disk anymore and must be approximated, e.g., by a least-squares Fourier approximation. The CROR model is checked against a time domain solution using rotating dipoles and validated with data from a test of Rolls-Royce's open rotor model rig 145 in DNW. The lowest three and most dominant peaks in the spectrum of the uninstalled rotor are well predicted by the method with errors less than 3dB with a correct directivity. For higher frequencies larger errors are observed. The CROR model has been developed for shielding calculations with the DLR BEM/FMM code. Some information about the code is given and the applicability of the model is demonstrated for a CROR installed at a modified DLR F6 aircraft geometry.

Contents

I	Introduction	4
II	The CROR Loading Noise Model	5
A	Pressure from a Loaded Surface	5
B	Pressure Field of CROR	6
C	Determination of CROR Frequencies	7
D	Single Ring Approximation of Loading Noise	8
III	Approximation of the Blade Loading Function	8
A	Unsteady Inflow Field of a Rotor	8
B	Introduction of the Difference Velocity	9
C	Single Blade Loading Function	9
D	Vaníček Approximation	9
E	Selection of the Frequencies	10
IV	Loading Noise in Time Domain	11
A	Determination of the Emitter Time	12
B	Calculation of the SPL	12
V	Rolls-Royce Rig 145 – 1/6th-Scale CROR	12
A	Approximated Blade Loading Function	14
B	CROR model and Time Domain SPL	14
C	Comparison with Experimental Data	14
VI	The Boundary Element Method (BEM)	17
VII	The Fast Multipole Method (FMM)	18
A	The Single-level FMM	20
B	The Multilevel FMM	20

^{*}Research Engineer, Department of Technical Acoustics, Institute of Aerodynamics and Flow Technology, German Aerospace Center (DLR), Lilienthalplatz 7, D-38108 Braunschweig

[†]Specialist Acoustics, Rolls-Royce Deutschland LTD & Co KG, Eschenweg 11, Dahlewitz, 15827 Blankenfelde-Mahlow

[‡]Head of the department of Technical Acoustics, Institute of Aerodynamics and Flow Technology, German Aerospace Center (DLR), Lilienthalplatz 7, D-38108 Braunschweig

VIII Rig 145 – Shielding Calculations	21
IX Summary and Conclusions	21
X Acknowledgements	22
References	22

List of Figures

1	CROR geometry of front (blue) and rear (green) rotor disk. One ring approximation of dipoles depicted.	5
2	Rotating line force on rotor disk	5
3	Direction of \mathbf{f} – View onto the rotor disk - z-component points out of plane	11
4	Rig 145 setup.	13
5	Rig 145 blade forces of front (left) and rear (right) rotor blade.	13
6	Vaníček approximation of axial and azimuthal component of Rig 145 force function on ring 4.	14
7	Vaníček spectrum of Rig 145 force functions on ring 4 of front and rear rotor. The modes are the combination of the two sets $\omega_m = m\bar{B}_k \left(\frac{\Omega_k}{\Omega_k} + 1 \right)$ and $\omega_j = j$. The peaks are near a multiple of about twice the blade number of the contra rotor.	15
8	Vaníček reconstruction of axial and azimuthal component of Rig 145 force function on ring 4.	15
9	Spectrum of Rig 145 using CROR model and time domain calculation in plane of front rotor. Mode numbers (m_0, m_1) .	16
10	Polar directivity of CROR model and time domain calculation for Rig 145 in plane of front rotor. Mode numbers (m_0, m_1) .	16
11	Azimuthal directivity of CROR model and time domain calculation for Rig 145 in plane of front rotor. Mode numbers (m_0, m_1) .	17
12	Measured and calculated spectrum and directivity	17
13	$N \log N$ scaling of the matrix-vector product in the range $10^3 \lesssim N \lesssim 10^7$ for monopole scattering at a sphere using the DLR FMM code.	22
14	1/6th-scale F6OR geometry with Rig 145 dipole rings and modulus of surface pressure. Mode $m_0 = 1, m_1 = 3$	22
15	Modulus of pressure in plane below 1/6th-scale F6OR geometry. CROR position near center, nose of aircraft points to the left.	23

Nomenclature

ξ	Source position.
ω	Angular frequency.
ω_j	Frequency of Vaníček polynomial
Ω_k	> 0 . Angular speed of rotor k .
$\bar{\Omega}_k$	> 0 . Angular speed of the contra-rotating rotor of rotor k .
\bar{B}_k	Blade number of contra-rotating rotor of rotor k .
ψ_E	$\pi \frac{\text{gcd}(B_0, B_1)}{B_0 B_1}$. Sound event difference angle.
Σ_k	Propeller disk of rotor k .
τ	Source time.
B_k	Blade number of rotor k .
α	Burton-Miller coupling constant
a_{0j}	Constant term of Vaníček polynomial
a_j	Cosine amplitude of Vaníček polynomial

b_j	Sine amplitude of Vaníček polynomial
$F_{bk,m}(\xi_k)$	Fourier (Vaníček) modes of blade loading function.
$F_{bk}(\xi_k, \tilde{\omega})$	Blade loading function in frequency domain.
$f_k(t)$	Point force (time domain loading noise)
m_q	Mach number vector of point force (time domain loading noise)
n_j	Normal vector of triangle j
$r(\tau)$	Distance between point force and observer (time domain loading noise)
T_j	Vaníček least-squares polynomial
x	Observer position.
x	Field point (can move into the wall)
y	Surface point
y_{jm}	Collocation points for the integration over the triangle j
$y_k(t)$	Path of point force (time domain loading noise)
$\Delta \tilde{f}_k(\xi_k, \tau)$	Disk loading function.
\hat{s}	Surface point on unit sphere
\hat{u}	Unit vector in u direction
$\tilde{F}_{bk}(\xi_k, \tau)$	Blade loading function in time domain.
$\tilde{p}_{Lk}(x, t)$	Acoustic pressure of rotor k due to loading noise as function of time.
$\tilde{p}_L(x, t)$	Loading noise in time domain.
\mathcal{A}	Surface of the scattering body
φ	Longitude coordinate on the unit sphere
ϑ	Co-latitude coordinate on the unit sphere
$A(x)$	Partial sum of an equation of the BEM system
$b_m(\vartheta)$	Co-latitude expansion functions
c	Sound speed.
$d\omega_s$	Surface element on unit sphere
$D_k(\phi, \tau)$	Drag (time domain loading noise)
$F(\varphi, \vartheta)$	Truncated surface-harmonic expansion on the unit sphere
$F_a(\hat{s})$	Far-field signature on the unit sphere centered in point a
$h_l^{(1)}(z)$	Spherical Hankel function of the first kind
i	imaginary unit $\sqrt{-1}$ or index
k	$= 0, 1$ Index of rotor or wave number.
k	Wave number
$L_k(\phi, \tau)$	Lift (time domain loading noise)

m_k	Vaníček Modes of front $k = 0$ and rear $k = 1$ rotor
$M_{L,\hat{s}}(\mathbf{u})$	FMM transfer function
M_{qr}	Projection of mach number vector of point force on $\mathbf{r}(\tau)$ (time domain loading noise)
$N_c(\hat{s})$	Near-field signature on the unit sphere centered in point c
p_{inc}	Incident pressure field
$P_l(x)$	Legendre polynomial
r	Radius on the rotor disk.
r	Distance between surface point and free-field point
S^2	Unit sphere
t	Observer time.
v_z	Velocity of point force along rotor axis for simulation of flight velocity.
W_m^j	Weights for the integration over the triangle j
$Y(\mathbf{y})$	Wall admittance
z_k	Axial position of rotor disk of rotor k .
$\tilde{G}(t, \tau; \mathbf{x}, \xi_k)$	Free-field Green's function of wave equation
$G(\mathbf{x}, \mathbf{y})$	Green's function used in BEM equation

I. Introduction

The recently increased interest in contra rotating open rotors (CROR) as alternative to turbofan engines has given rise to noise concerns and stimulated the exploration of effects of shielding by the aircraft geometry. For low Mach numbers it is believed that the influence of the flight velocity can be neglected and the problem can be tackled approximately as scattering problem for the Helmholtz equation. The most efficient way to solve the Helmholtz equation are the Boundary Element Method (BEM) or its accelerated variant, the Fast Multipole Method (FMM). The BEM/FMM integral equation is usually solved in the Burton-Miller [1] formulation which guarantees uniqueness of the solution for all frequencies. Besides the incident pressure on the scattering surface, the Burton-Miller approach requires knowledge of the normal derivative of the incident field on the surface. Therefore, an appropriate analytical model for the pressure field of the CROR in frequency domain must be supplied. A simple model for the loading noise of a propeller has been given by Glegg [2]. There, the loading noise is approximated in frequency domain by a sum of dipoles distributed on circles on the propeller disk. The dipole strengths are related to the blade forces which can be obtained from CFD calculations. This model has been extended to CRORs with identical rotational speeds of both rotors by Müller [3]. Generally, however, the rotors of a CROR have different rotational speeds which must be taken into account appropriately. In the present paper the CROR loading noise model of [2, 3] is extended to the case of CRORs with different rotational speeds. Then, generally, the blade forces are no longer periodic in the rotor disk. Since unsteady CFD calculations of CRORs are very expensive and thus can be performed for only very few revolutions (e.g., one or two) of the rotors, the blade forces must be reconstructed appropriately. For this task a least-squares Fourier approximation proposed by Vaníček [4, 5] has been found useful.

This paper is structured as follows. First, the CROR model for loading noise will be presented. Then, details of the least-squares Fourier approximation of the blade loading function are given. The time domain solution for the loading noise model follows. The theory is then applied to the Rig 145 1/6th-scale CROR designed and tested by Rolls-Royce. For the most intense frequencies good agreement with experimental data from the DNW is found. Finally, a brief overview of the DLR FMM code used for shielding calculations is given, and an example of a scattering calculation of an installed CROR is presented.

II. The CROR Loading Noise Model

Glegg [2] assumes that the load distribution on each blade of the propeller can be represented by a point loading at a suitable spanwise location. Consequently, he models the propeller acoustically by a dipole source rotating in a circle on the propeller disk. A radial load distribution can be taken into account by rotating dipoles on several circles. While it is possible to consider non-planar rotor disks and curved blades, for convenience the following discussion is restricted to straight blades rotating in a plane.

The CROR consists of two contra-rotating rotors distinguished by the index $k = 0, 1$, cf. Fig. 1. The axis of the CROR is the z -axis pointing into flight direction. The front rotor has the index $k = 0$ and is located at position z_0 . The rear rotor has the index $k = 1$ and is located at position z_1 . The blade numbers of the rotors are denoted by B_k and the angular frequencies by Ω_k . The blade number and angular velocity of the complementary rotor of rotor k are denoted by \bar{B}_k and $\bar{\Omega}_k$ (thus, it is $\bar{B}_0 = B_1, \bar{B}_1 = B_0, \bar{\Omega}_0 = \Omega_1, \bar{\Omega}_1 = \Omega_0$). The angular velocities are defined to be always positive, i.e., $\Omega_k > 0$.

A. Pressure from a Loaded Surface

Following Glegg [2], the loading noise $\tilde{p}_{Lk}(\mathbf{x}, t)$ created by an unsteady force distribution $\Delta \tilde{f}_k(\xi_k, \tau)$ on a rotor disk Σ_k is given by

$$\tilde{p}_{Lk}(\mathbf{x}, t) = \int_{-T}^T d\tau \int_{\Sigma_k} d\xi_k \Delta \tilde{f}_k(\xi_k, \tau) \cdot \nabla_{\xi} \tilde{G}(t, \tau; \mathbf{x}, \xi_k). \quad (1)$$

In the uninstalled case (i.e., no scattering objects are present), $\tilde{G}(t, \tau; \mathbf{x}, \xi_k)$ is the free-field Green's function of the wave equation

$$\tilde{G}(t, \tau; \mathbf{x}, \xi_k) = \frac{\delta(\tau - t + \frac{r_k}{c})}{4\pi r_k}, \quad r_k \equiv |\mathbf{x} - \xi_k|. \quad (2)$$

Here, c is the sound speed, τ and ξ_k are the source time and position and t and \mathbf{x} are the observer time and position. The source point ξ_k is located on the propeller disk Σ_k and reads in cylindrical coordinates

$$\xi_k(r, \phi, z_k) = \begin{pmatrix} r \cos \phi \\ r \sin \phi \\ z_k \end{pmatrix}. \quad (3)$$

$\Delta \tilde{f}_k(\xi_k, \tau)$ is also called the disk loading function. The disk loading function of a superposition of B_k single blades rotating with an angular velocity Ω_k is connected with the blade loading function $\tilde{F}_{bk}(\xi_k, \tau)$ by

$$\Delta \tilde{f}_k(\xi_k, \tau) = \sum_{b=0}^{B_k-1} \sum_{n=-\infty}^{\infty} \tilde{F}_{bk}(\xi_k, \tau) \delta\left(\phi - \Omega_k \tau - \frac{2\pi b}{B_k} + 2\pi n\right). \quad (4)$$

The delta function produces a line source rotating with angular velocity Ω_k , cf. Fig. 2. In order to take into account also rotors of different rotational speeds, in extension of the work of Glegg, the blade loading function $\tilde{F}_{bk}(\xi_k, \tau)$ is assumed not only to be a function of the position ξ_k on the rotor disk, but also to be a function of time τ . Therefore, a Fourier integral ansatz seems to be appropriate

$$\tilde{F}_{bk}(\xi_k, \tau) = \int_{-\infty}^{\infty} d\tilde{\omega} e^{-i\tilde{\omega}\tau} F_{bk}(\xi_k, \tilde{\omega}). \quad (5)$$

The inverse transform is given by

$$F_{bk}(\xi_k, \tilde{\omega}) = \frac{1}{2\pi} \int_{-\infty}^{\infty} d\tau e^{i\tilde{\omega}\tau} \tilde{F}_{bk}(\xi_k, \tau). \quad (6)$$

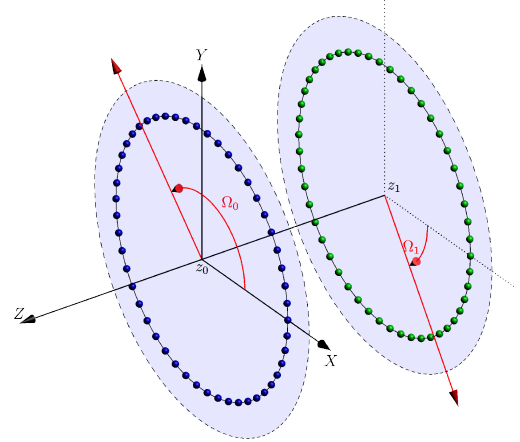


Figure 1. CROR geometry of front (blue) and rear (green) rotor disk. One ring approximation of dipoles depicted.

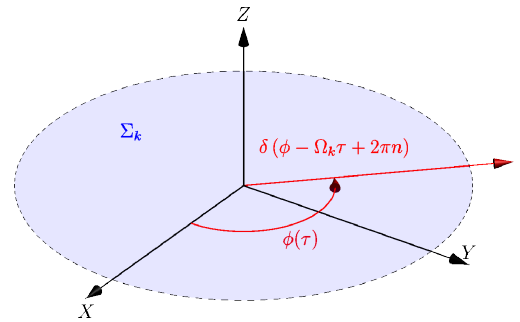


Figure 2. Rotating line force on rotor disk

The disk loading function of a superposition of B_k single blades rotating with an angular velocity Ω_k now becomes

$$\Delta \tilde{f}_k(\xi_k, \tau) = \sum_{b=0}^{B_k-1} \sum_{n=-\infty}^{\infty} \int_{-\infty}^{\infty} d\tilde{\omega} F_{bk}(\xi_k, \tilde{\omega}) e^{-i\tilde{\omega}\tau} \delta\left(\phi - \Omega_k \tau - \frac{2\pi b}{B_k} + 2\pi n\right). \quad (7)$$

Applying the Poisson summation formula^a on the summation over n yields

$$\Delta \tilde{f}_k(\xi_k, \tau) = \frac{1}{2\pi} \sum_{b=0}^{B_k-1} \int_{-\infty}^{\infty} d\tilde{\omega} F_{bk}(\xi_k, \tilde{\omega}) e^{-i\tilde{\omega}\tau} \sum_{n=-\infty}^{\infty} e^{in\left(\phi - \Omega_k \tau - \frac{2\pi b}{B_k}\right)}. \quad (8)$$

Now it is convenient to introduce the frequency abbreviation

$$\omega_n \equiv \tilde{\omega} + n\Omega_k \quad (9)$$

and write for the disk loading function

$$\Delta \tilde{f}_k(\xi_k, \tau) = \frac{1}{2\pi} \sum_{b=0}^{B_k-1} \int_{-\infty}^{\infty} d\tilde{\omega} F_{bk}(\xi_k, \tilde{\omega}) \sum_{n=-\infty}^{\infty} e^{in\left(\phi - \frac{2\pi b}{B_k}\right)} e^{-i\omega_n \tau}. \quad (10)$$

B. Pressure Field of CROR

Substituting the disk loading function Eq. (10) into the pressure integral Eq. (1), the loading noise of rotor k becomes

$$\tilde{p}_{Lk}(\mathbf{x}, t) = -\frac{1}{2\pi} \int_{\Sigma_k} d\xi_k \sum_{b=0}^{B_k-1} \int_{-\infty}^{\infty} d\tilde{\omega} F_{bk}(\xi_k, \tilde{\omega}) \cdot \nabla_{\mathbf{x}} \int_{-T}^T d\tau \sum_{n=-\infty}^{\infty} e^{in\left(\phi - \frac{2\pi b}{B_k}\right)} e^{-i\omega_n \tau} \tilde{G}(t, \tau; \mathbf{x}, \xi_k). \quad (11)$$

One concludes from the free-field Green's function Eq. (2) that the integrand of Eq. (11) is only different from zero for $\tau = t - \frac{r_k}{c}$. After substitution of the free-field Green's function Eq. (2) and integration over τ , one obtains

$$\tilde{p}_{Lk}(\mathbf{x}, t) = -\frac{1}{2\pi} \int_{\Sigma_k} d\xi_k \sum_{b=0}^{B_k-1} \int_{-\infty}^{\infty} d\tilde{\omega} F_{bk}(\xi_k, \tilde{\omega}) \cdot \nabla_{\mathbf{x}} \sum_{n=-\infty}^{\infty} e^{-i\omega_n t} e^{in\left(\phi - \frac{2\pi b}{B_k}\right)} \frac{e^{i\omega_n \frac{r_k}{c}}}{4\pi r_k}. \quad (12)$$

After a Fourier transform^b with respect to time t , it follows

$$p_{Lk}(\mathbf{x}, \omega) = \int_{-\infty}^{\infty} d\tilde{\omega} \sum_{n=-\infty}^{\infty} -\delta(\omega - \omega_n) \sum_{b=0}^{B_k-1} \int_{\Sigma_k} d\xi_k e^{in\left(\phi - \frac{2\pi b}{B_k}\right)} F_{bk}(\xi_k, \tilde{\omega}) \cdot \nabla_{\mathbf{x}} \frac{e^{i\omega_n \frac{r_k}{c}}}{4\pi r_k} \quad (14)$$

where ω is the frequency. Using $\nabla_{\mathbf{x}} = -\nabla_{\xi}$ for the derivatives of the Green's function gives

$$p_{Lk}(\mathbf{x}, \omega) = \sum_{n=-\infty}^{\infty} \int_{-\infty}^{\infty} d\tilde{\omega} \delta(\omega - \omega_n) \sum_{b=0}^{B_k-1} \int_{\Sigma_k} d\xi_k e^{in\left(\phi - \frac{2\pi b}{B_k}\right)} F_{bk}(\xi_k, \tilde{\omega}) \cdot \nabla_{\xi} \frac{e^{i\omega_n \frac{r_k}{c}}}{4\pi r_k}. \quad (15)$$

The integrand of the integral over $\tilde{\omega}$ is different from zero only for $\omega = \omega_n$. From Eq. (9) one has $\tilde{\omega} = \omega - n\Omega_k$ and obtains for the loading noise

$$p_{Lk}(\mathbf{x}, \omega) = \sum_{n=-\infty}^{\infty} \sum_{b=0}^{B_k-1} \int_{\Sigma_k} d\xi_k e^{in\left(\phi - \frac{2\pi b}{B_k}\right)} F_{bk}(\xi_k, \omega - n\Omega_k) \cdot \nabla_{\xi} \frac{e^{i\omega \frac{r_k}{c}}}{4\pi r_k}. \quad (16)$$

^a Poisson's sum formula reads (here is $T = 2\pi$)

$$\sum_{n=-\infty}^{\infty} \delta(t - Tn) = \frac{1}{T} \sum_{n=-\infty}^{\infty} e^{2\pi i n \frac{t}{T}}$$

^b The Fourier transform is defined as

$$p_{Lk}(\mathbf{x}, \omega) = \int_{-\infty}^{\infty} \tilde{p}_{Lk}(\mathbf{x}, t) e^{i\omega t} dt, \quad \tilde{p}_{Lk}(\mathbf{x}, t) = \frac{1}{2\pi} \int_{-\infty}^{\infty} p_{Lk}(\mathbf{x}, \omega) e^{-i\omega t} d\omega \quad (13)$$

A relation for the different rotational directions can be obtained by substituting $\Omega_k \rightarrow \pm\Omega_k$ and reversing the summation over n . The general formula for both rotation directions then becomes

$$p_{Lk}(\mathbf{x}, \omega) = \sum_{n=-\infty}^{\infty} \sum_{b=0}^{B_k-1} \int_{\Sigma_k} d\xi_k e^{\pm i n \left(\phi - \frac{2\pi b}{B_k} \right)} \mathbf{F}_{bk}(\xi_k, \omega - n\Omega_k) \cdot \nabla_{\xi} \frac{e^{i\omega \frac{r_k}{c}}}{4\pi r_k}. \quad (17)$$

An ansatz for the blade loading function and its Fourier transform is (cf. section A)

$$\tilde{\mathbf{F}}_{bk}(\xi_k, \tau) = \sum_{m=-\infty}^{\infty} e^{\pm i m \bar{B}_k (\bar{\Omega}_k - \Omega_k) \tau} \mathbf{F}_{bk,m}(\xi_k), \quad (18)$$

$$\mathbf{F}_{bk}(\xi_k, \tilde{\omega}) = \sum_{m=-\infty}^{\infty} \mathbf{F}_{bk,m}(\xi_k) \delta(\tilde{\omega} \pm m \bar{B}_k (\bar{\Omega}_k - \Omega_k)). \quad (19)$$

After substitution the loading noise becomes

$$p_{Lk}(\mathbf{x}, \omega) = \sum_{n=-\infty}^{\infty} \sum_{m=-\infty}^{\infty} \delta(\omega - n\Omega_k \pm m \bar{B}_k (\bar{\Omega}_k - \Omega_k)) \sum_{b=0}^{B_k-1} \int_{\Sigma_k} d\xi_k e^{\pm i n \left(\phi - \frac{2\pi b}{B_k} \right)} \times \\ \times \mathbf{F}_{bk,m}(\xi_k) \cdot \nabla_{\xi} \frac{e^{i\omega \frac{r_k}{c}}}{4\pi r_k}. \quad (20)$$

C. Determination of CROR Frequencies

The pressure field of the CROR is a superposition of the pressure field of the two single rotors $k = 0, 1$

$$p_L(\mathbf{x}, \omega) = p_{L0}(\mathbf{x}, \omega) + p_{L1}(\mathbf{x}, \omega) \quad (21)$$

where

$$p_{Lk}(\mathbf{x}, \omega) = \sum_{n_k=-\infty}^{\infty} \sum_{m_k=-\infty}^{\infty} \delta(\omega - n_k \Omega_k \pm m_k \bar{B}_k (\bar{\Omega}_k - \Omega_k)) \sum_{b=0}^{B_k-1} \int_{\Sigma_k} d\xi_k e^{\pm i n_k \left(\phi - \frac{2\pi b}{B_k} \right)} \times \\ \times \mathbf{F}_{bk,m_k}(\xi_k) \cdot \nabla_{\xi} \frac{e^{i\omega \frac{r_k}{c}}}{4\pi r_k}, \quad k = 0, 1. \quad (22)$$

This equation is the complete point spectrum of the CROR and contains infinitely many frequencies. Usually, one is interested in the pressure for a single frequency ω and has to determine the proper terms n_k, m_k of the double sums which belong to ω . For the frequency ω the sums do not vanish for

$$\omega = n_k \Omega_k \mp m_k \bar{B}_k (\bar{\Omega}_k - \Omega_k) = (n_k \pm m_k \bar{B}_k) \Omega_k \mp m_m \bar{B}_k \bar{\Omega}_k. \quad (23)$$

Examining the delta functions of p_{L0} and p_{L1} , one obtains

$$\omega = (n_0 \mp m_0 B_1) \Omega_0 \pm m_0 B_1 \Omega_1, \quad (24)$$

$$\omega = (n_1 \mp m_1 B_0) \Omega_1 \pm m_1 B_0 \Omega_0. \quad (25)$$

In order to determine the values n_k, m_k both equations are subtracted

$$(n_0 \mp m_0 B_1 \mp m_1 B_0) \Omega_0 + (\pm m_0 B_1 - n_1 \pm m_1 B_0) \Omega_1 = 0. \quad (26)$$

Since this equation must hold for arbitrary Ω_k one obtains the equations

$$n_0 \mp m_0 B_1 \mp m_1 B_0 = 0, \quad (27)$$

$$n_1 \mp m_0 B_1 \mp m_1 B_0 = 0. \quad (28)$$

The modes n_k for the rotors are therefore

$$n_k = \pm(m_0 B_1 + m_1 B_0). \quad (29)$$

One sees that the modes n_k are the same for both rotors. Substituting $n = n_k$, the frequency becomes

$$\omega = \pm(m_1 B_0 \Omega_0 + m_0 B_1 \Omega_1). \quad (30)$$

One can use the positive sign for frequency and mode and obtains

$$\begin{aligned} \omega &= m_1 B_0 \Omega_0 + m_0 B_1 \Omega_1, \quad n = m_0 B_1 + m_1 B_0 \\ p_L(\mathbf{x}, \omega) &= \sum_{b=0}^{B_0-1} \int_{\Sigma_0} d\xi_0 e^{\pm i n \left(\phi - \frac{2\pi b}{B_0} \right)} \mathbf{F}_{b0, m_0}(\xi_0) \cdot \nabla_{\xi} \frac{e^{i \omega \frac{r_0}{c}}}{4\pi r_0} + \\ &+ \sum_{b=0}^{B_1-1} \int_{\Sigma_1} d\xi_1 e^{\mp i n \left(\phi - \frac{2\pi b}{B_1} \right)} \mathbf{F}_{b1, m_1}(\xi_1) \cdot \nabla_{\xi} \frac{e^{i \omega \frac{r_1}{c}}}{4\pi r_1}. \end{aligned} \quad (31)$$

After selection of the two Fourier modes m_0, m_1 , the frequency ω , mode number n , and pressure $p_L(\mathbf{x}, \omega)$ of the CROR are determined.

D. Single Ring Approximation of Loading Noise

The integrals for the loading noise Eq. (20) can quite well be approximated by one or more 'effective rings'. That means that the blade loading function as function of the radius r can be concentrated at discrete values r_q of the radius. For example, the loading noise for rotor k in a single ring approximation ($\xi_{kj} = \xi(r_q, \phi_j, z_k)$) becomes

$$p_{Lk}(\mathbf{x}, \omega) = \sum_{n=-\infty}^{\infty} \delta(\omega - \omega_n) \sum_{b=0}^{B_k-1} \sum_{j=0}^{N-1} \Delta\phi e^{\pm i n \left(\phi_j - \frac{2\pi b}{B_k} \right)} \mathbf{F}_{bk}(\xi_{kj}) \cdot \nabla_{\xi} \frac{e^{i \frac{\omega}{c} |\mathbf{x} - \xi_{kj}|}}{4\pi |\mathbf{x} - \xi_{kj}|}. \quad (32)$$

The plus and minus sign in the exponential function distinguishes the two possible rotation directions of the rotor.

III. Approximation of the Blade Loading Function

The blade loading function $\tilde{F}_{bk}(\xi_k, \tau)$, Eq. (18), for the determination of the loading noise is input to the CROR model. It can be determined from unsteady CFD simulations. In the following, a suitable ansatz for $\tilde{F}_{bk}(\xi_k, \tau)$ is given and its determination from CFD data using a least-squares Fourier approximation is described.

A. Unsteady Inflow Field of a Rotor

It is assumed that the rotor k rotates in positive ϕ direction and the contra-rotating rotor in negative ϕ direction. The coordinate system is *airframe fixed*. While in steady flight a *single* rotor has usually a steady inflow field, a rotor of a CROR has *always unsteady inflow* conditions. Thus, an ansatz for the unsteady blade force on the rotor disk is (using cylindrical coordinates $\xi_k = (r, \phi, z_k)$)

$$\tilde{F}_{bk}(\xi_k, \tau) = \sum_{m=-\infty}^{\infty} a_{km}(\xi_k) e^{i m \bar{B}_k (\phi + \bar{\Omega}_k \tau)}. \quad (33)$$

The coefficients a_{k0} can describe the steady part of the inflow field, which can be distorted, e.g., by the airframe or an angle of attack. The coefficients $a_{km}, |m| > 0$ describe the rotating part of the inflow field caused by the contra-rotating rotor. The azimuthal phase speed of these modes is $-\bar{\Omega}_k$, i.e., the modes move synchronous with the contra-rotating rotor in negative ϕ direction. The relation between blade angle ϕ and time τ is

$$\phi(\tau) = \Omega_k \tau. \quad (34)$$

Thus the blade 'sees' the force

$$\tilde{F}_{bk}(\xi_k, \tau) = \sum_{m=-\infty}^{\infty} a_{km} e^{i m \bar{B}_k ((\bar{\Omega}_k + \Omega_k) \tau)}. \quad (35)$$

Using the angle ϕ one can also write

$$\tilde{F}_{bk}\left(\xi_k, \frac{\phi}{\Omega_k}\right) = \sum_{m=-\infty}^{\infty} a_{km} e^{i m \bar{B}_k \left(\frac{\bar{\Omega}_k}{\Omega_k} + 1 \right) \phi}. \quad (36)$$

In case of same rotational speeds of both rotors, i.e. $\bar{\Omega}_k/\Omega_k = 1$, only integer wave numbers appear in the argument of the exponential function and the blade loading function can be approximated by a classical Fourier polynomial in ϕ . In the general case, the coefficients a_{km} can be obtained by least-squares spectral analysis following Vaníček (cf. section D).

B. Introduction of the Difference Velocity

In Eq. (18) the blade loading function was written using the difference velocity $\bar{\Omega}_k - \Omega_k$. This can be introduced into Eq. (35) using the identity $\Omega_k \tau = -\Omega_k \tau + 2\phi$ which yields

$$\sum_m a_{km} e^{im\bar{B}_k(\bar{\Omega}_k + \Omega_k)\tau} = \sum_m a_{km} e^{im\bar{B}_k(\bar{\Omega}_k - \Omega_k)\tau + 2im\bar{B}_k\phi}. \quad (37)$$

Thus, one has the following representations of the blade loading function

$$\begin{aligned} \tilde{F}_{bk}(\xi_k, \tau) &= \sum_{m=-\infty}^{\infty} a_{km} e^{im\bar{B}_k(\bar{\Omega}_k + \Omega_k)\tau}, \\ &= \sum_{m=-\infty}^{\infty} a_{km} e^{im\bar{B}_k 2\phi} e^{im\bar{B}_k(\bar{\Omega}_k - \Omega_k)\tau} \end{aligned} \quad (38)$$

The Fourier modes $F_{bk,m}(\xi_k)$ in Eq. (18) can now be defined by

$$F_{bk,m}(\xi_k) \equiv a_{km}(\xi_k) e^{im\bar{B}_k 2\phi} \quad (39)$$

and, introducing again the proper sign for positive and negative rotation direction, Eq. (18) is recovered

$$\tilde{F}_{bk}(\xi_k, \tau) = \sum_{m=-\infty}^{\infty} e^{\pm im\bar{B}_k(\bar{\Omega}_k - \Omega_k)\tau} F_{bk,m}(\xi_k). \quad (40)$$

C. Single Blade Loading Function

Generally, every blade b has its own loading function $\tilde{F}_{bk}(\xi_k, \tau)$. For simplicity, it is often assumed that the loading function $\tilde{F}_{bk}(\xi_k, \tau)$ can be approximated by an appropriately shifted loading function from a single blade, $\tilde{F}_{bk}(r, \phi, z_k; \tau) = \tilde{F}_k(r, \phi + \psi_b, z_k; \tau)$, where ψ_b is an appropriate shift angle. It is, for example, possible to use for the angle ψ_b the first angular position where the blade b of rotor k coincides with a blade of the contra-rotating rotor. These angles ψ_b are multiples of the so-called sound event difference angle

$$\psi_E \equiv \pi \frac{\gcd(B_0, B_1)}{B_0 B_1}. \quad (41)$$

It is also possible to set directly $\psi_b = \pm b\psi_E$, where the positive sign applies to a rotor rotating in mathematically positive direction.

D. Vaníček Approximation

The single blade loading function is obtained from full CFD simulations of the CROR. Since these unsteady simulations are extremely expensive, only data of one (or only very few) revolutions of the rotors can be calculated. In case of a ϕ -periodic load function (same rotational speeds of both rotors), this is sufficient. In the general case, however, one faces the difficult problem to reconstruct a non-periodic function from only some relatively short samples. Least-squares spectral analysis developed by Vaníček [4, 5] or alternatively [6] can be applied for this task. There, a Fourier approximation using appropriately chosen frequencies is constructed from only limited samples of the function. This removes the restrictions of the periodicity implied in classical analysis using Fourier series.

The Vaníček-approximation is a method for spectral analysis of signals using successive least-squares fits. Given data points $(\phi_i, f_i = f(\phi_i))$, $i = 0, 1, \dots, n-1$, the key idea is to determine a frequency ω_j and perform a least-squares fit of the data with the function

$$T_j(\phi) = a_{0j} + a_j \cos \omega_j \phi + b_j \sin \omega_j \phi \quad (42)$$

After determination of a_{0j} , a_j , and b_j , the function $T_j(\phi)$ is subtracted from the original data $f(\phi_i)$ and the procedure is repeated for another frequency ω_{j+1} on the reduced data set. After M steps of this procedure, one has a Fourier approximation of the form

$$f(\phi) \approx \sum_{j=0}^{M-1} a_{0j} + \sum_{j=0}^{M-1} a_j \cos \omega_j \phi + \sum_{j=0}^{M-1} b_j \sin \omega_j \phi \quad (43)$$

Vaníček [4] gives a method for the determination of the frequencies that assures convergence of the method. In case of the loading function of a CROR, the frequencies ω_j are known in advance. One set of frequencies is obtained from the blade number and shaft speed of the contra-rotating rotor, and another set are the usual integer wave numbers of periodic function approximation. It is important to note that the Vaníček algorithm that is formulated in [4] for scalar data works also for vector valued functions.

Now a brief sketch of the least-squares approximation for a vector valued function follows. It is assumed that n data points (ϕ_i, \mathbf{f}_i) , $i = 0, 1, \dots, n-1$ with $-\pi \leq \phi_i \leq \pi$

$$\phi_i = -\pi + 2\pi \frac{i}{n-1}, \quad i = 0, 1, \dots, n-1 \quad (44)$$

are given. A frequency ω_j , $j = 0$ is chosen and using the ansatz

$$T_j(\phi) = a_{0j} + a_j \cos \omega_j \phi + b_j \sin \omega_j \phi \quad (45)$$

the least-squares equations become

$$\begin{pmatrix} \sum_{i=0}^{n-1} 1 & \sum_{i=0}^{n-1} \cos \omega_j \phi_i & \sum_{i=0}^{n-1} \sin \omega_j \phi_i \\ \sum_{i=0}^{n-1} \cos \omega_j \phi_i & \sum_{i=0}^{n-1} \cos^2 \omega_j \phi_i & \sum_{i=0}^{n-1} \sin \omega_j \phi_i \cos \omega_j \phi_i \\ \sum_{i=0}^{n-1} \sin \omega_j \phi_i & \sum_{i=0}^{n-1} \cos \omega_j \phi_i \sin \omega_j \phi_i & \sum_{i=0}^{n-1} \sin^2 \omega_j \phi_i \end{pmatrix} \begin{pmatrix} a_{0j} \\ a_j \\ b_j \end{pmatrix} = \begin{pmatrix} \sum_{i=0}^{n-1} f_i \\ \sum_{i=0}^{n-1} f_i \cos \omega_j \phi_i \\ \sum_{i=0}^{n-1} f_i \sin \omega_j \phi_i \end{pmatrix}. \quad (46)$$

Now, one has for all $\omega_j \in \mathbb{R}$ the relations $\sum_{i=0}^{n-1} \sin \omega_j \phi_i = 0$ and $\sum_{i=0}^{n-1} \sin \omega_j \phi_i \cos \omega_j \phi_i = 0$. With definition of

$$Q \equiv \sum_{i=0}^{n-1} \cos \omega_j \phi_i, \quad Q_1 \equiv \sum_{i=0}^{n-1} \cos^2 \omega_j \phi_i, \quad Q_2 \equiv \sum_{i=0}^{n-1} \sin^2 \omega_j \phi_i \quad (47)$$

the least-squares equations become

$$\begin{pmatrix} n & Q & 0 \\ Q & Q_1 & 0 \\ 0 & 0 & Q_2 \end{pmatrix} \begin{pmatrix} a_{0j} \\ a_j \\ b_j \end{pmatrix} = \begin{pmatrix} \sum_{i=0}^{n-1} f_i \\ \sum_{i=0}^{n-1} f_i \cos \omega_j \phi_i \\ \sum_{i=0}^{n-1} f_i \sin \omega_j \phi_i \end{pmatrix}. \quad (48)$$

Thus, the coefficients of the approximation are

$$a_{0j} = \frac{1}{n} \left(\sum_{i=0}^{n-1} f_i - a_j Q \right), \quad a_j = \frac{n \sum_{i=0}^{n-1} f_i \cos \omega_j \phi_i - Q \sum_{i=0}^{n-1} f_i}{nQ_1 - Q^2}, \quad b_j = \frac{\sum_{i=0}^{n-1} f_i \sin \omega_j \phi_i}{Q_2}. \quad (49)$$

After determination of the coefficients for the frequency ω_j the approximation Eq. (45) is subtracted from the data values \mathbf{f}_i

$$\mathbf{f}_i \leftarrow \mathbf{f}_i - T_j(\phi_i) \quad (50)$$

and the least-squares fit for the next frequency ω_{j+1} is performed.

E. Selection of the Frequencies

Like mentioned above, for same rotational speeds $\Omega_k = \bar{\Omega}_k$, the loading function can be approximated by a Fourier polynomial using integer frequencies. In case of $\Omega_k \neq \bar{\Omega}_k$ also frequencies appearing in Eq. (36) must be considered. It was found to be important to remove the frequencies with the largest amplitudes first. Thus, the first set of frequencies consists of the frequencies from Eq. (36)

$$\omega_0 = 1\bar{B}_k \left(\frac{\bar{\Omega}_k}{\Omega_k} + 1 \right), \quad \omega_1 = 2\bar{B}_k \left(\frac{\bar{\Omega}_k}{\Omega_k} + 1 \right), \quad \dots, \quad \omega_{M-2} = (M-1)\bar{B}_k \left(\frac{\bar{\Omega}_k}{\Omega_k} + 1 \right). \quad (51)$$

The second set of frequencies are the standard (integer) Fourier modes

$$\omega_{M-1} = 1, \quad \omega_M = 2, \quad \omega_{M+1} = 3, \quad \dots, \quad \omega_{M+N-3} = N-1. \quad (52)$$

The numbers of frequencies M, N must be specified appropriately.

IV. Loading Noise in Time Domain

The basis of the CROR model presented above is the sound field generated by a planar distribution of unsteady forces. This planar distribution can be concentrated on one or more circles (or rings) on the rotor disk. In case of moving point forces, it is possible to solve the underlying wave equation directly. Thus, it is possible to compare the CROR model with a time domain solution of point forces rotating on the same circles. Moreover, in time domain it is possible to take into account a flight velocity by translation of the forces along the rotor axis. The position of a point force on a circle (or a screw in case of an additional translation) of rotor k is denoted by $\mathbf{y}_k(t)$. The pressure field $\tilde{p}_{Lk}(\mathbf{x}, t)$ of a point force $\mathbf{f}_k(t)$ moving along $\mathbf{y}_k(t)$ is then obtained from the inhomogeneous wave equation

$$\frac{1}{c_0^2} \frac{\partial^2 \tilde{p}_{Lk}}{\partial t^2} - \Delta \tilde{p}_{Lk} = -\nabla [\delta(\mathbf{x} - \mathbf{y}_k(t)) \mathbf{f}_k(t)]. \quad (53)$$

The solution is^c

$$\tilde{p}_{Lk}(\mathbf{x}, t) = \frac{1}{4\pi r(1 - M_{qr})^2} \left[\frac{1}{c_0} \left(\frac{\partial \mathbf{f}_k}{\partial \tau} \cdot \mathbf{e}_r + \frac{\mathbf{f}_k \cdot \mathbf{e}_r}{1 - M_{qr}} \left(\frac{\partial \mathbf{m}_q}{\partial \tau} \cdot \mathbf{e}_r \right) \right) + \frac{1}{r} \left(-(\mathbf{f}_k \cdot \mathbf{m}_q) + (1 - m_q^2) \frac{\mathbf{f}_k \cdot \mathbf{e}_r}{1 - M_{qr}} \right) \right] \quad (54)$$

where

$$\mathbf{r}(\tau) = \mathbf{x} - \mathbf{y}_k(\tau), \quad \mathbf{e}_r = \frac{\mathbf{r}}{r}, \quad \mathbf{m}_q = \frac{1}{c_0} \frac{d\mathbf{y}_k}{d\tau}, \quad M_{qr} = \mathbf{m}_q \cdot \mathbf{e}_r \quad (55)$$

$\mathbf{r}(\tau)$ is the vector between the observer point \mathbf{x} and the source point $\mathbf{y}_k(\tau)$. The relation between the receiver time t and the emitter time τ is

$$g(\tau) = \tau - t + \frac{|\mathbf{r}(\tau)|}{c_0} = 0 \quad (56)$$

from which the function $\tau(t)$ has to be calculated.

Now it is assumed that the point force rotates at distance r_q around the z -axis with angular velocity Ω_k and translates parallel to the z -axis with velocity v_z . Let the angular position of the force with initial angle ϕ_b be $\phi(\tau) = \Omega_k \tau + \phi_b$. Then, the position $\mathbf{y}_k(\tau)$ of the force and its derivatives are

$$\mathbf{y}_k(\tau) = r_q \begin{pmatrix} \cos \phi \\ \sin \phi \\ z_k + v_z \tau \end{pmatrix}, \quad \frac{d\mathbf{y}_k}{d\tau} = r_q \Omega_k \begin{pmatrix} -\sin \phi \\ \cos \phi \\ v_z \end{pmatrix}, \quad \frac{d^2 \mathbf{y}_k}{d\tau^2} = r_q \Omega_k^2 \begin{pmatrix} -\cos \phi \\ -\sin \phi \\ 0 \end{pmatrix} \quad (57)$$

For convenience the (small) radial component of the force is neglected and only lift (i.e. thrust acting in z -direction) and drag (acting azimuthally) are considered. The force vector is then defined as (see also the Fig. 3)

$$\mathbf{f} = \begin{pmatrix} f_x \\ f_y \\ f_z \end{pmatrix} = \begin{pmatrix} -D_k \sin \phi \\ +D_k \cos \phi \\ +L_k \end{pmatrix} \quad (58)$$

where $L_k(\phi, \tau)$ and $D_k(\phi, \tau)$ are the lift and drag of the rotor blade generally depending on position and time. The drag components f_x, f_y point into the rotation direction of the rotor, and the lift component f_z into the flight direction. In case of a rotor rotating in positive direction, the drag D_k is negative, i.e. $D_k < 0$.

The force \mathbf{f}_k is the force on the fluid and thus equal to $-\mathbf{f}$. Thus, one obtains for the point force and its derivative

$$\mathbf{f}_k(\tau) = \begin{pmatrix} +D_k(\phi, \tau) \sin \phi \\ -D_k(\phi, \tau) \cos \phi \\ -L_k(\phi, \tau) \end{pmatrix} \quad (59)$$

$$\frac{\partial \mathbf{f}_k}{\partial \tau} = \begin{pmatrix} + \left(\frac{\partial D_k(\phi, \tau)}{\partial \tau} + \Omega_k \frac{\partial D_k(\phi, \tau)}{\partial \phi} \right) \sin \phi \\ - \left(\frac{\partial D_k(\phi, \tau)}{\partial \tau} + \Omega_k \frac{\partial D_k(\phi, \tau)}{\partial \phi} \right) \cos \phi \\ - \left(\frac{\partial L_k(\phi, \tau)}{\partial \tau} + \Omega_k \frac{\partial L_k(\phi, \tau)}{\partial \phi} \right) \end{pmatrix} + \Omega_k \begin{pmatrix} +D_k(\phi, \tau) \cos \phi \\ +D_k(\phi, \tau) \sin \phi \\ 0 \end{pmatrix}. \quad (60)$$

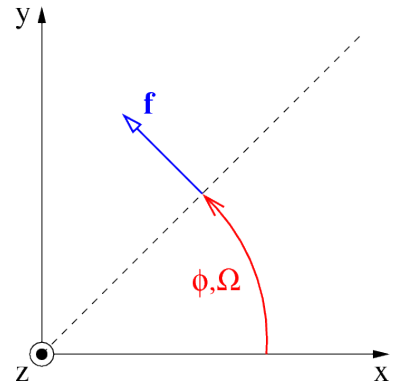


Figure 3. Direction of \mathbf{f} - View onto the rotor disk - z -component points out of plane

^cSee, e.g., the lecture notes: [J.Delfs, Notes_Basics_Aeroacoustics_Delfs.pdf](#)

A. Determination of the Emitter Time

The emitter time $\tau(t)$ as function of observer time is obtained by solution of the implicit equation

$$g(\tau) = \tau - t + \frac{|\mathbf{r}(\tau)|}{c_0} = 0. \quad (61)$$

The distance between source and observer is

$$\mathbf{r}(\tau) = \mathbf{x} - \mathbf{y}_k(\tau) = \mathbf{x} - \begin{pmatrix} r_q \cos(\Omega\tau + \phi_b) \\ r_q \sin(\Omega\tau + \phi_b) \\ z_k + v_z\tau \end{pmatrix}. \quad (62)$$

Writing $\mathbf{x} = (x, y, z)^T$ one obtains

$$|\mathbf{r}(\tau)| = \sqrt{\mathbf{x}^2 + (r_q^2 + z_k^2 + 2z_kv_z\tau + v_z^2\tau^2) - 2r_q [x \cos(\Omega_k\tau + \phi_b) + y \sin(\Omega_k\tau + \phi_b)] - 2z(z_k + v_z\tau)}. \quad (63)$$

The derivative of $g(\tau)$ becomes

$$\frac{dg}{d\tau} = 1 + \frac{\Omega_k r_q}{c_0} \frac{x \sin(\Omega_k\tau + \phi_b) - y \cos(\Omega_k\tau + \phi_b)}{|\mathbf{r}(\tau)|} + \frac{z_k v_z + v_z^2\tau - z v_z}{c_0 |\mathbf{r}(\tau)|}. \quad (64)$$

Now one can set up the Newton procedure

$$\begin{aligned} \tau^{n+1} &= \tau^n - \frac{g(\tau^n)}{g'(\tau^n)} \\ &= \tau^n - \frac{\tau^n - t + \frac{|\mathbf{r}(\tau^n)|}{c_0}}{1 + \frac{\Omega_k r_q}{c_0} \frac{x \sin(\Omega_k\tau^n + \phi_b) - y \cos(\Omega_k\tau^n + \phi_b)}{|\mathbf{r}(\tau^n)|} + \frac{z_k v_z + v_z^2\tau^n - z v_z}{c_0 |\mathbf{r}(\tau^n)|}}. \end{aligned} \quad (65)$$

As initial value one can choose

$$\tau^0 = t - \frac{|\mathbf{r}_0|}{c_0}, \quad \mathbf{r}_0 = (x, y, z - z_k - v_z t)^T. \quad (66)$$

B. Calculation of the SPL

For an observer point \mathbf{x} and time t the pressure $\tilde{p}_{Lk}(\mathbf{x}, t)$, Eq. (54), are calculated for every blade and circle of the CROR and added, giving the acoustic pressure $\tilde{p}_L(\mathbf{x}, t)$. Like for the CROR model the single blade loading function must be shifted for every blade by a multiple of the sound event difference angle [3], Eq. (41), i.e., one sets for blade b of rotor k for the lift and drag

$$L_k(\phi, \tau) \longrightarrow L_k(\phi \pm b\psi_E, \tau) \quad (67)$$

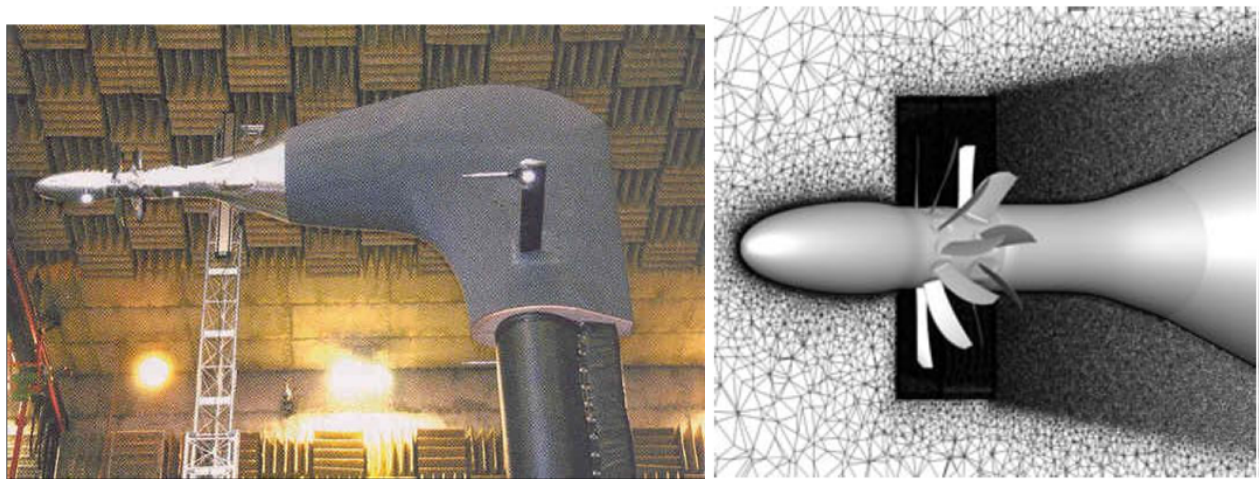
$$D_k(\phi, \tau) \longrightarrow D_k(\phi \pm b\psi_E, \tau) \quad (68)$$

The functions $L_k(\phi, \tau)$ and $D_k(\phi, \tau)$ are the axial and azimuthal components of the blade loading function $\tilde{\mathbf{F}}_{bk}(\xi_k, \tau)$, cf. Eq. (33). In order to calculate the sound pressure level (SPL) for every observer point, a time sequence of pressure values $p_L(\mathbf{x}, t_i)$, $t_i = i\Delta t$, $i = 0, 1, \dots, N-1$ is calculated and a subsequent Fast Fourier Transform gives the SPL.

V. Rolls-Royce Rig 145 – 1/6th-Scale CROR

Rig 145 is a 1/6th-scale model CROR which has been designed and evaluated experimentally by Rolls-Royce. Fig. 4a shows the installation of the Rig 145 CROR by Rolls-Royce in the open test section of the Large Dutch-German Wind tunnel (DNW). Some design parameters are (index 0 front rotor, 1 rear rotor) $B_0 = 12$, $B_1 = 9$. The CROR is cropped, i.e., the diameter of the rear rotor is smaller than that of the front rotor.

The single blade loading function has been obtained from unsteady RANS calculations [9]. Fig. 4b shows the unstructured mesh for the calculations using the DLR TAU code [8]. Fig. 5 depicts the axial and azimuthal components of the blade loading function for the front and rear rotor. The significantly larger oscillations of the forces on the rear rotor are caused by the wakes of the front rotor blades. The front rotor, however, is influenced only by small potential perturbations induced upstream by the rear rotor.



a) Uninstalled counter rotating open rotor at the DNW test facility. From [7] b) CFD Mesh for the URANS simulation of the CROR. From [8]

Figure 4. Rig 145 setup.

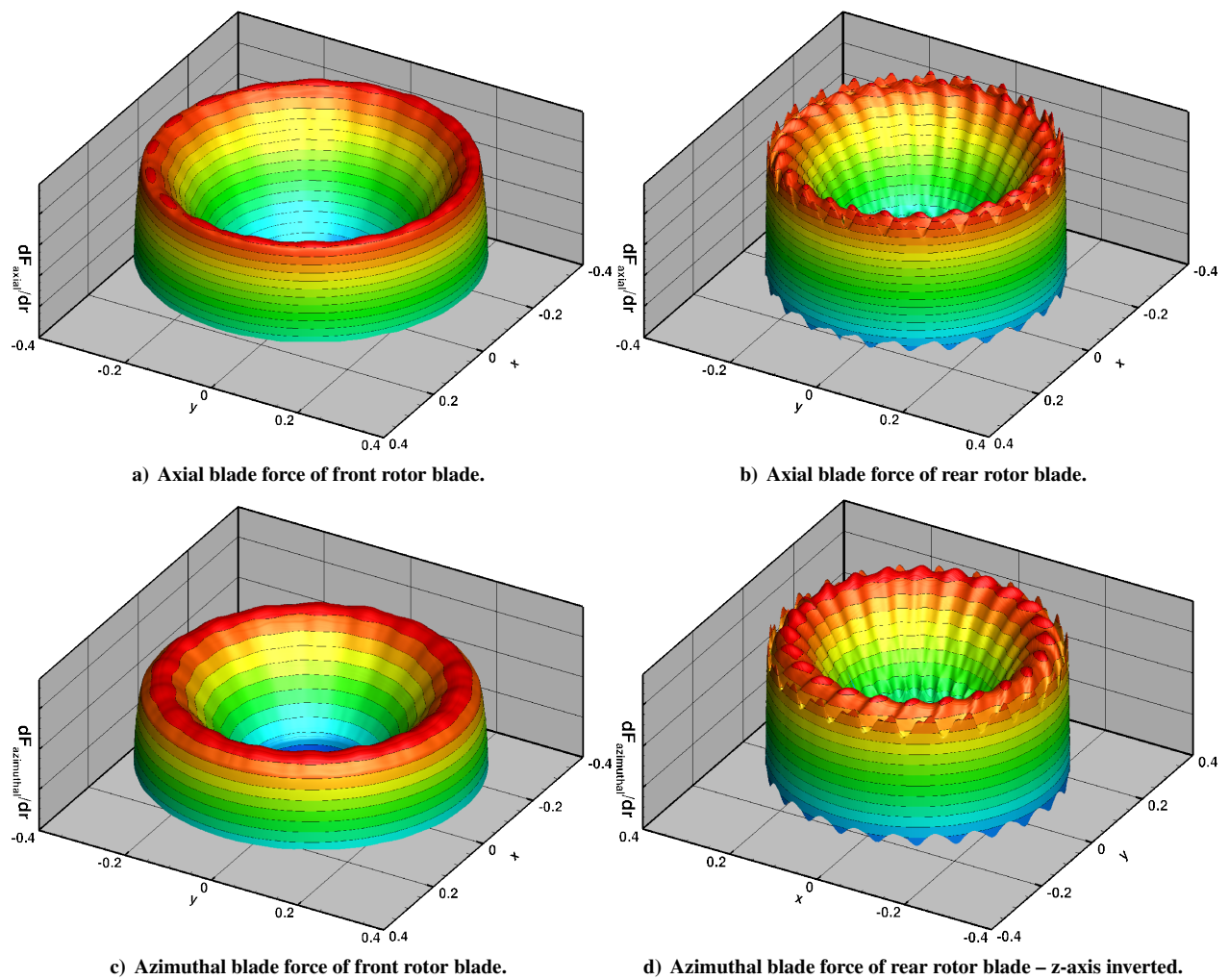


Figure 5. Rig 145 blade forces of front (left) and rear (right) rotor blade.

A. Approximated Blade Loading Function

The single blade loading function, cf. Fig. 5, is given for only about one revolution of the rotors. This loading function is lumped together by integration to point forces defined on 6 circles on each rotor disk. The point forces on the 6 rings are then approximated by a Vaníček approximation.

Fig. 6 depicts the Vaníček approximation of the axial and azimuthal component of the force function on ring 4 for the front and rear rotor. The black circles are the original force function and the red and blue lines the approximated ones. One sees, that the least-squares Fourier fit approximates the force function very well.

Fig. 7 shows the spectrum of the force function on ring 4 for the front and rear rotor. According to Eq. (51) and Eq. (52) the modes (or frequencies) are the combination of the two sets $\omega_m = m\bar{B}_k\left(\frac{\Omega_k}{\Omega_k} + 1\right)$ and $\omega_j = j$. Since every rotor 'sees' the disturbances of its contra rotor, the front rotor force has its maxima near multiples of twice the rear rotor blade number, whereas the rear rotor force has its maxima near multiples of twice the front rotor blade number. Fig. 8 shows the reconstructed signal for 3 revolutions of the rotors. No artefacts due to the interval boundaries of the data are visible.

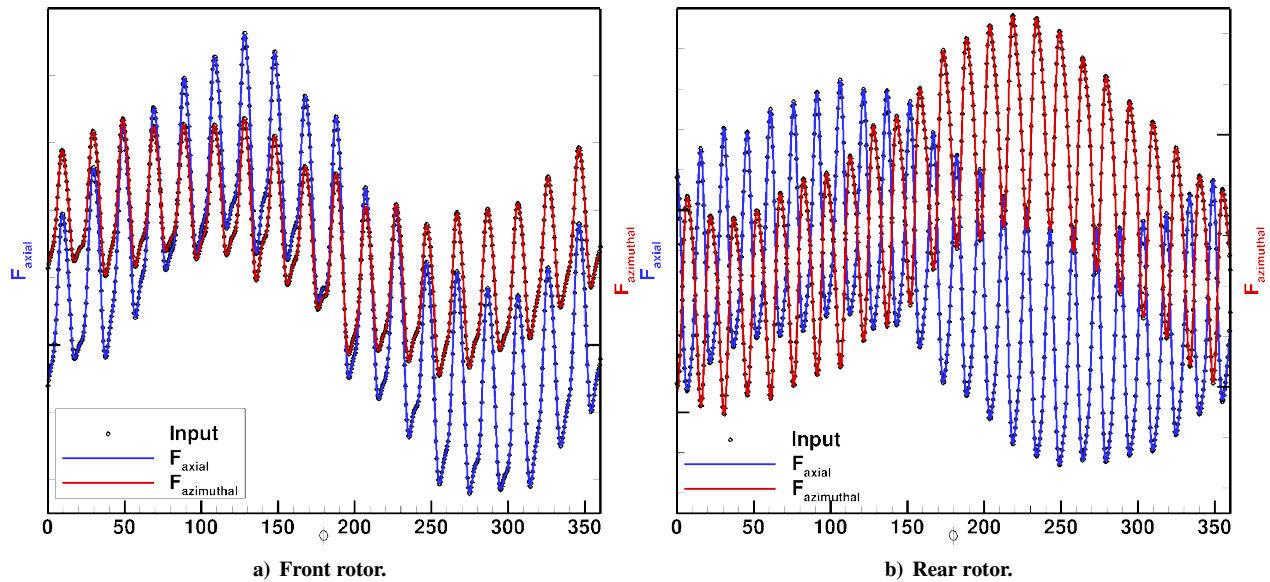


Figure 6. Vaníček approximation of axial and azimuthal component of Ring 145 force function on ring 4.

B. CROR model and Time Domain SPL

Fig. 9 depicts the spectrum of the CROR model in comparison with the time domain spectrum of rotating point forces. For modes belonging to the upper 20 dB of the spectrum the agreement between frequency- and time-domain solution is quite good.

Fig. 10 shows the polar and Fig. 11 the azimuthal directivity for the most important modes of the CROR model and the rotating point forces. Again the coincidence between CROR model and time domain calculation is quite good.

C. Comparison with Experimental Data

Fig. 12a and Fig. 12b show the comparison of the CROR model to the experimental data obtained with the uninstalled open rotor model in the Large Dutch-German Wind tunnel (DNW).

The measured data shown in the picture have been corrected and scaled to a unit distance from the open rotor. As described above, the CROR model is formulated only for the frequencies of the tones of the open rotor. Currently no broadband noise is modelled. Therefore, the validation with the experimental data can only be performed for the tonal peaks in the spectrum.

Fig. 12a shows the spectrum of a microphone in the rotor plane of the first rotor in comparison to the CROR model prediction at the same position. As can be seen from the figure, the first three CROR tones match very well in

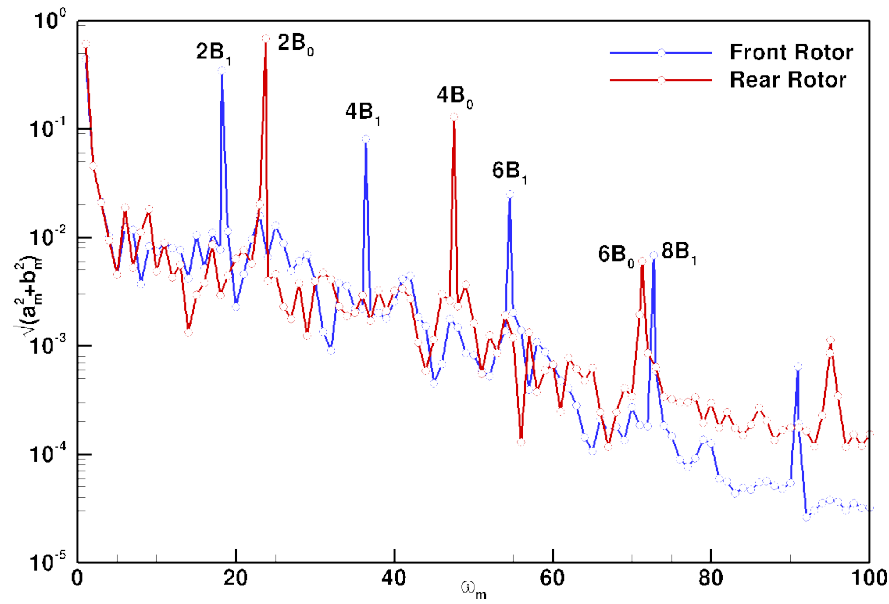


Figure 7. Vaníček spectrum of Rig 145 force functions on ring 4 of front and rear rotor. The modes are the combination of the two sets $\omega_m = m\bar{B}_k \left(\frac{\bar{\Omega}_k}{\bar{\Omega}_k} + 1 \right)$ and $\omega_j = j$. The peaks are near a multiple of about twice the blade number of the contra rotor.

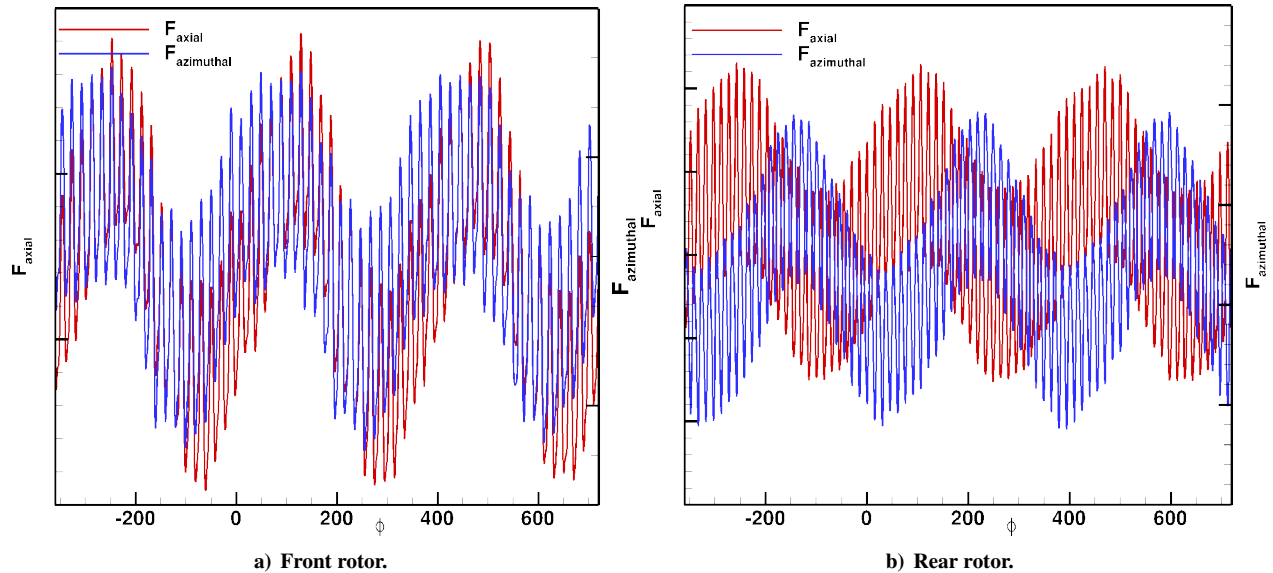


Figure 8. Vaníček reconstruction of axial and azimuthal component of Rig 145 force function on ring 4.

amplitude. The dominant low frequency peaks in the spectrum are very well predicted with an error of less than 3 dB for the whole process chain.

With increasing frequency the measured amplitude of the CROR tones decreases and the measured peaks broaden in the spectrum. Such effects are not present in the CROR model prediction. In consequence the tone levels are more and more overpredicted by the method with increasing frequency. It is assumed, that this discrepancy is at least partially caused by the attenuation of tones in the wind tunnel experiment due to the interaction of the radiated noise with the shear layer turbulence of the wind tunnel. This effect is only present in the wind tunnel configuration and not in flight. Therefore, it is considered as a measurement error of the wind tunnel test. Another possible cause for the observed mismatch at higher frequencies that cannot be ruled out currently is the approximation of the two rotors by straight blades. Further investigation is required to understand the mismatch of prediction and experimental data for

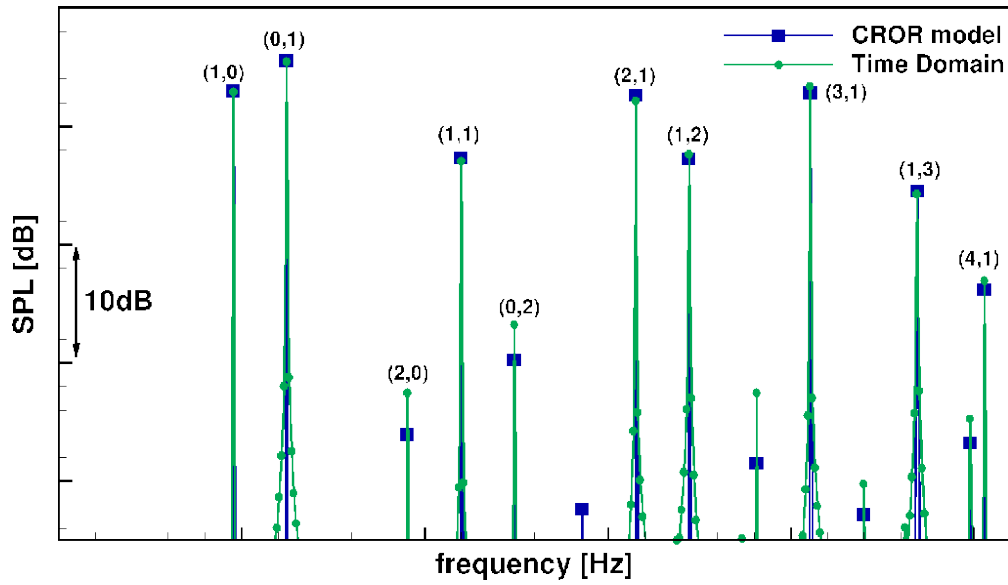


Figure 9. Spectrum of Rig 145 using CROR model and time domain calculation in plane of front rotor. Mode numbers (m_0, m_1) .

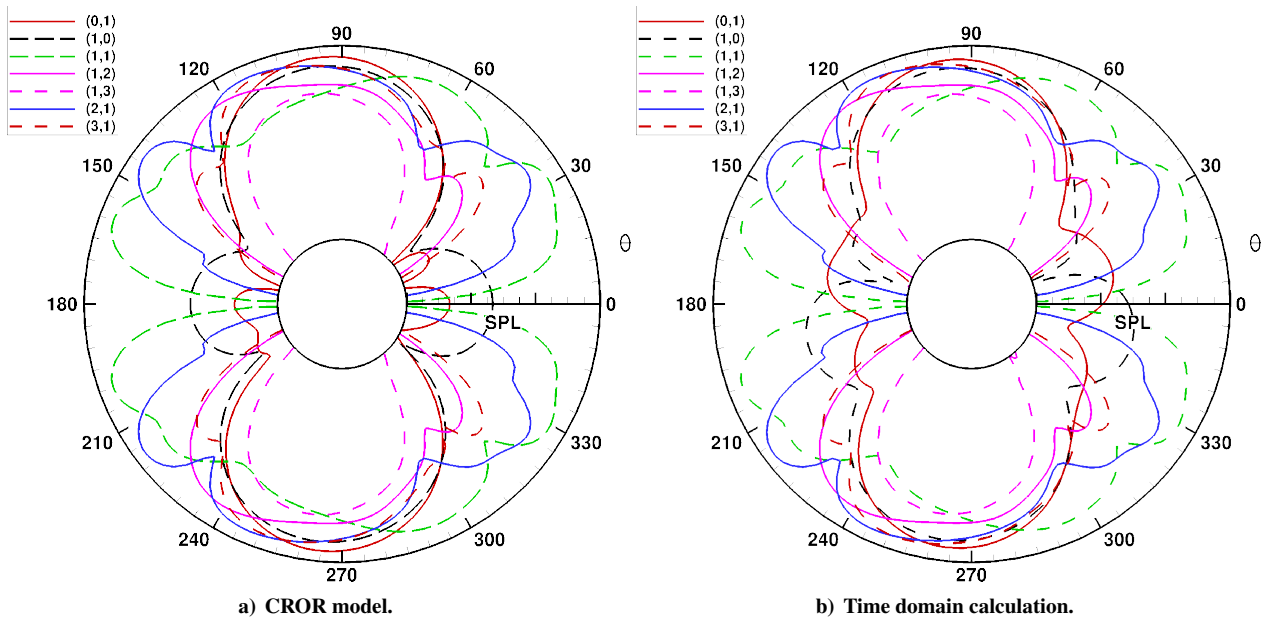


Figure 10. Polar directivity of CROR model and time domain calculation for Rig 145 in plane of front rotor. Mode numbers (m_0, m_1) .

higher frequencies.

Fig. 12b shows the directivity of the dominant tone in the low frequency spectrum due to the blade passing frequency of the front rotor. The peak frequency at an emission angle of 90 degrees is well predicted. For comparison the experimental data is plotted over the physical emission angle. The CROR model prediction is based on an observer in a medium at rest. The directivity is well predicted. The error is below 3dB even though the flow condition differs between wind tunnel and model assumptions.

Altogether, the presented comparison with experimental data validates the whole tool chain from the CFD over the extraction and spectral approximation of equivalent sources for the CROR model from the limited length time series to the far-field evaluation.

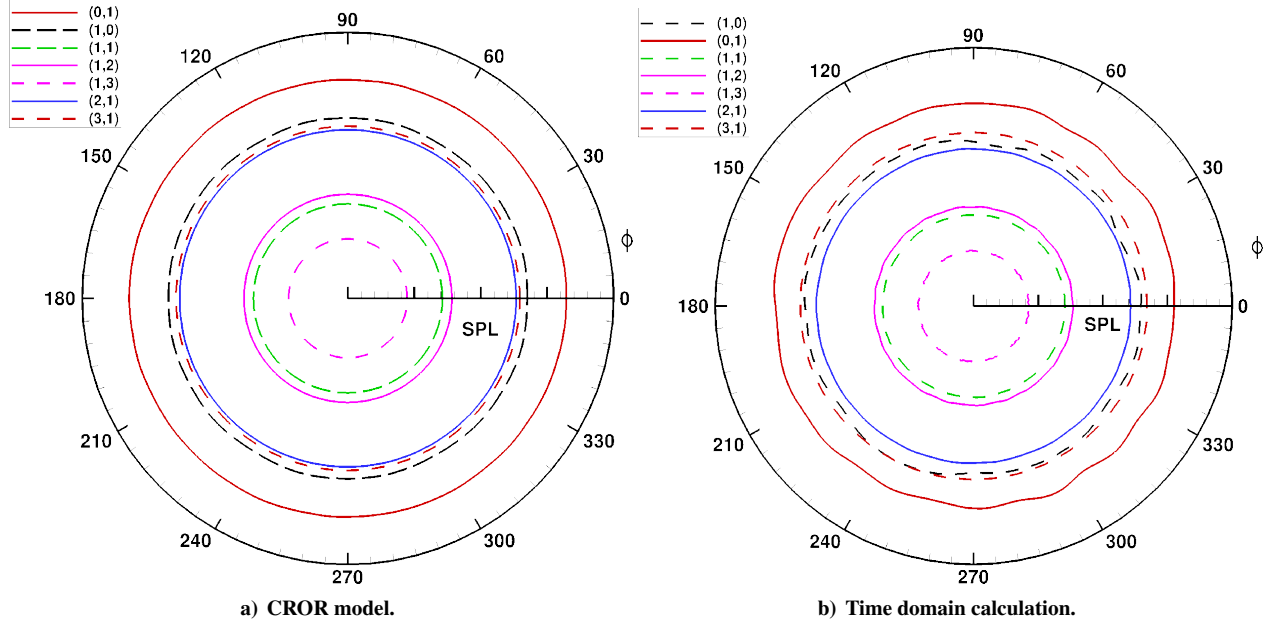


Figure 11. Azimuthal directivity of CROR model and time domain calculation for Rig 145 in plane of front rotor. Mode numbers (m_0, m_1) .

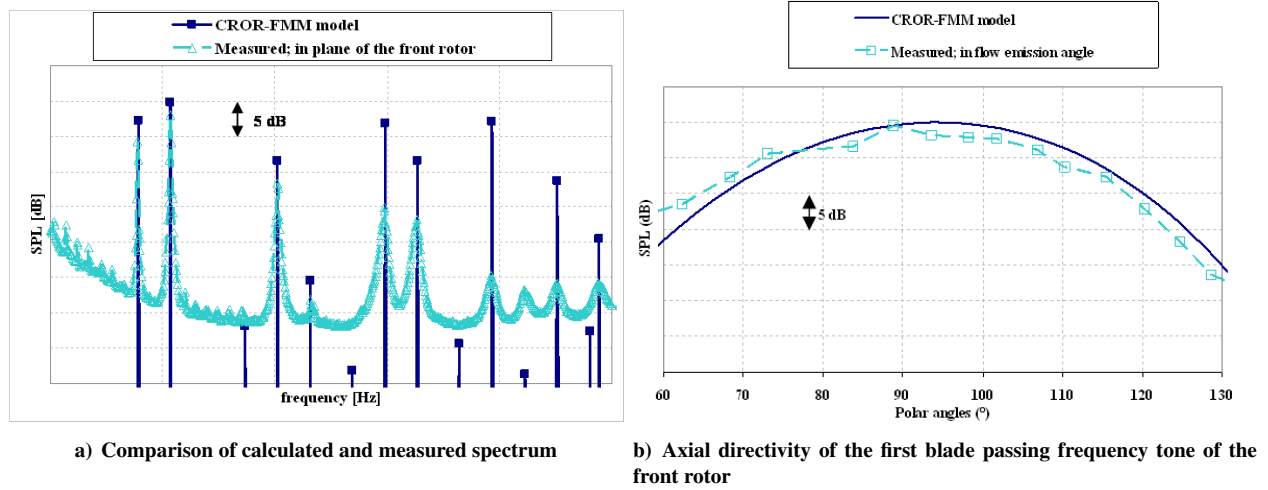


Figure 12. Measured and calculated spectrum and directivity

VI. The Boundary Element Method (BEM)

The CROR model has been designed for application in shielding calculations. For small Mach numbers acoustic shielding can be considered as a scattering problem for the Helmholtz equation. The most efficient solution procedures for this type of problems are based on boundary integral equations.

In the following, the basic integral equation for scattering problems will be given. This integral equation is the same for the boundary element method (BEM) and the fast multipole method (FMM). Only the solution procedure differs.

The sound field $p(\mathbf{x})$ which is produced by an incident field $p_{inc}(\mathbf{x})$ scattered at a body with the surface \mathcal{A} obeys the equation (see, e.g., [1, 10])

$$c p(\mathbf{x}) = p_{inc}(\mathbf{x}) + \frac{1}{4\pi} \int_{\mathcal{A}} \left[p(\mathbf{y}) \frac{\partial G(\mathbf{x}, \mathbf{y})}{\partial n_y} - \frac{\partial p(\mathbf{y})}{\partial n_y} G(\mathbf{x}, \mathbf{y}) \right] d\mathcal{A}_y, \quad (69)$$

where $G(\mathbf{x}, \mathbf{y})$ is the free-field Green's function

$$G(\mathbf{x}, \mathbf{y}) = \frac{e^{ikr}}{r}, \quad r^2 = (\mathbf{x} - \mathbf{y})^2. \quad (70)$$

The incident pressure field is denoted by $p_{inc}(\mathbf{x})$ and is calculated in case of CROR shielding by Eq. (31). The constant c equals 1 if the point \mathbf{x} is in the free field (i.e. away from the body) and equals $\frac{1}{2}$ if the point \mathbf{x} is on the (smooth) surface \mathcal{A} . k is the wave number of the sound field and i the imaginary unit. In order to obtain an integral equation for the surface pressure, it is convenient to relate the pressure gradient on the surface $\frac{\partial p(\mathbf{y})}{\partial n_y}$ to the pressure $p(\mathbf{y})$ by introduction of a given wall admittance Y

$$\frac{\partial p(\mathbf{y})}{\partial n_y} = Y(\mathbf{y})p(\mathbf{y}). \quad (71)$$

The wall admittance is zero at solid walls. Substitution of Eq. (71) into Eq. (69) yields for a point \mathbf{x} on the surface

$$\frac{1}{2}p(\mathbf{x}) - \frac{1}{4\pi} \int_{\mathcal{A}} p(\mathbf{y}) \left[\frac{\partial}{\partial n_y} - Y \right] G(\mathbf{x}, \mathbf{y}) d\mathcal{A}_y = p_{inc}(\mathbf{x}) \quad (72)$$

Unfortunately, the solution of this equation is not unique if the wave number k is an eigenvalue of the inner problem of the body with surface \mathcal{A} . A possible solution to this uniqueness problem is to consider a linear combination of Eq. (72) and a normal derivative with respect to \mathbf{x} (cf. [1]). This so-called Burton-Miller approach is equivalent to the application of the operator $\left[1 + \alpha \frac{\partial}{\partial n_x}\right]$ to Eq. (72). One obtains

$$\frac{1}{2} [1 + \alpha Y(\mathbf{x})] p(\mathbf{x}) - \frac{1}{4\pi} \int_{\mathcal{A}} p(\mathbf{y}) \left[\frac{\partial}{\partial n_y} - Y \right] \left[1 + \alpha \frac{\partial}{\partial n_x} \right] G(\mathbf{x}, \mathbf{y}) d\mathcal{A}_y = \left[1 + \alpha \frac{\partial}{\partial n_x} \right] p_{inc}(\mathbf{x}). \quad (73)$$

α is the Burton-Miller coupling constant with $\Im(\alpha) \neq 0$. A common choice for α is

$$\alpha = \frac{i}{k} \quad (74)$$

This choice is nearly optimal for sphere-like objects [11, 12].

In the classical BEM approach, the scattering surface can be discretized, e.g., into triangles. Assuming a constant pressure on every triangle and choosing appropriate collocation points [13], the integrals over the triangles can be evaluated and a system of linear equations for the surface pressure values is obtained. Details can be found in [14].

The system of linear equations can be solved using direct or iterative solvers. In any case, the matrix which is complex and fully occupied must be stored. Since a resolution of at least six elements per wavelength λ are necessary the number of unknowns for a body with surface A is larger $N \approx 6^2 \frac{A}{\lambda^2}$ and the number of matrix elements scales like λ^{-4} . This leads to prohibitively large memory requirements for small wavelengths and limits the classical BEM approach to low frequencies. In order to overcome this bottleneck, Fast Multipole Methods (FMM) have been developed.

VII. The Fast Multipole Method (FMM)

The Fast Multipole Method [15–21]. uses an iterative solver and thus relies on the fast evaluation of matrix-vector products. The complexity of the product can be reduced from $O(N^2)$ to $O(N \log N)$. FMM algorithms come in some flavours and consist of many parts and it is not possible to give any significant amount of details here. As far as the author^d is aware of, the DLR FMM code differs essentially in the multilevel interpolation algorithm from implementations described in the literature and thus it deemed to be sufficient to elucidate only those parts of the algorithm which are necessary to understand the chosen interpolation.

In order to highlight the basic ideas of the FMM, the i -th equation of the discretized form of Eq. (73) is written in the form

$$\sum_{j=0}^{N-1} p_j B(\mathbf{y}_i, \mathbf{y}_j) \equiv b(\mathbf{y}_i). \quad (75)$$

Now, any part of the sum over the triangles j is denoted by $A(\mathbf{x}) = \sum_j p_j B(\mathbf{x}, \mathbf{y}_j)$. For this brief overview only the following typical term of the sum $A(\mathbf{x})$ is discussed

$$A(\mathbf{x}) = \sum_j p(\mathbf{y}_j) \sum_m w_m^j \frac{\partial G(\mathbf{x}, \mathbf{y}_{jm})}{\partial n_y} + \dots \quad (76)$$

^dM.Lummer

y_{jm} and W_m^j are some collocation points and weights of the integration over the triangle j . In the DLR FMM code the so-called plane wave approximation has been implemented and the following discussion is based on a paper of J.Rahola [18]. In the plane wave approximation the Green's function is represented by the following integral over the unit sphere S^2

$$G(\mathbf{x}, \mathbf{y}) = \frac{e^{ik|\mathbf{x}-\mathbf{y}|}}{|\mathbf{x}-\mathbf{y}|} \approx \frac{ik}{4\pi} \int_{S^2} e^{ik\hat{\mathbf{s}} \cdot (\mathbf{x}-\mathbf{c})} M_{L,\hat{\mathbf{s}}}(\mathbf{c}-\mathbf{a}) e^{ik\hat{\mathbf{s}} \cdot (\mathbf{a}-\mathbf{y})} d\omega_{\hat{\mathbf{s}}},$$

$$|\mathbf{c}-\mathbf{a}| > |(\mathbf{x}-\mathbf{c}) + (\mathbf{a}-\mathbf{y})|, \quad (77)$$

$$M_{L,\hat{\mathbf{s}}}(\mathbf{u}) \equiv \sum_{l=0}^L (2l+1) i^l h_l^{(1)}(ku) P_l(\hat{\mathbf{s}} \cdot \hat{\mathbf{u}}), \quad \mathbf{u} = u\hat{\mathbf{u}}, \quad |\hat{\mathbf{u}}| = 1. \quad (78)$$

$\hat{\mathbf{s}}$ is the (unit) vector to a point of the sphere and $d\omega_{\hat{\mathbf{s}}}$ a surface element of the sphere. Some remarks are advisable. First, it is important to note that the two points \mathbf{x} and \mathbf{y} of which the distance appear in the argument of the Green's function are separated into two exponential functions under the integral sign. Thus, any differential operator in \mathbf{x} or \mathbf{y} acting on the Green's function becomes diagonal under the integral, i.e., it results in straightforward multiplications of the integrand with some power of $ik\hat{\mathbf{s}}$. Furthermore, two arbitrary points \mathbf{a} and \mathbf{c} have been introduced which can be specified appropriately. The numerical expenditures have been shifted into the so-called transfer function $M_{L,\hat{\mathbf{s}}}(\mathbf{c}-\mathbf{a})$, which is a finite sum over products of Hankel functions and Legendre polynomials and depends for a fixed point on the sphere only on the difference $\mathbf{c}-\mathbf{a}$. The limit $\lim_{L \rightarrow \infty} M_{L,\hat{\mathbf{s}}}(\mathbf{u})$ is divergent and the cutoff value L must be chosen carefully [22]. Unfortunately, it is not possible here to discuss this topic further.

Substitution of the representation Eq. (77) into the sum Eq. (76) yields the approximation

$$A(\mathbf{x}) = \frac{k^2}{4\pi} \int_{S^2} e^{ik\hat{\mathbf{s}} \cdot (\mathbf{x}-\mathbf{c})} \sum_j p_j \sum_m M_{L,\hat{\mathbf{s}}}(\mathbf{c}-\mathbf{a}) W_j^m \mathbf{n}_j \cdot \hat{\mathbf{s}} e^{ik\hat{\mathbf{s}} \cdot (\mathbf{a}-\mathbf{y}_{jm})} d\omega_{\hat{\mathbf{s}}}. \quad (79)$$

\mathbf{n}_j is the normal vector of the triangle j . Now the points \mathbf{a} and \mathbf{c} are specified. Setting $\mathbf{c} = \mathbf{x}$ in Eq. (79) allows the definition of the so-called far-field signature $F_a(\hat{\mathbf{s}})$

$$A(\mathbf{x}) = \frac{k^2}{4\pi} \int_{S^2} M_{L,\hat{\mathbf{s}}}(\mathbf{x}-\mathbf{a}) \underbrace{\sum_j p_j \sum_m W_j^m \mathbf{n}_j \cdot \hat{\mathbf{s}} e^{ik\hat{\mathbf{s}} \cdot (\mathbf{a}-\mathbf{y}_{jm})} d\omega_{\hat{\mathbf{s}}}}_{\equiv F_a(\hat{\mathbf{s}})}, \quad |\mathbf{x}-\mathbf{a}| > |\mathbf{y}_{jm}-\mathbf{a}|. \quad (80)$$

The far-field signature $F_a(\hat{\mathbf{s}})$ contains the information of the sum of the triangles near \mathbf{a} . For calculation of $A(\mathbf{x})$, the point \mathbf{x} must be *outside* the source region.

Setting $\mathbf{a} = \mathbf{y}_{jm}$ in Eq. (79) allows the definition the so-called near-field signature $N_c(\hat{\mathbf{s}})$

$$A(\mathbf{x}) \approx \frac{k^2}{4\pi} \int_{S^2} e^{ik\hat{\mathbf{s}} \cdot (\mathbf{x}-\mathbf{c})} \underbrace{\sum_j p_j \sum_m M_{L,\hat{\mathbf{s}}}(\mathbf{c}-\mathbf{y}_{jm}) W_j^m \mathbf{n}_j \cdot \hat{\mathbf{s}} d\omega_{\hat{\mathbf{s}}}}_{\equiv N_c(\hat{\mathbf{s}})}, \quad |\mathbf{x}-\mathbf{c}| < |\mathbf{y}_{jm}-\mathbf{c}|. \quad (81)$$

The near-field signature $N_c(\hat{\mathbf{s}})$ contains the information of the sum of the triangles near \mathbf{c} . For calculation of $A(\mathbf{x})$ the point \mathbf{x} must be *inside* the source region.

From the signatures $F_a(\hat{\mathbf{s}})$ and $N_c(\hat{\mathbf{s}})$, one can calculate the sum $A(\mathbf{x})$ by evaluation of the sphere integrals Eq. (80) and Eq. (81) for $|\mathbf{x}-\mathbf{a}| > R$ and $|\mathbf{x}-\mathbf{a}| < R$, i.e., outside and inside of a source region with radius $R = |\mathbf{y}_{jm}-\mathbf{a}|$. Usually, the near-field signature is not calculated by its definition, because it involves the (costly) evaluation of the transfer function. For $|\mathbf{x}-\mathbf{a}| < R$ it is much cheaper to evaluate $A(\mathbf{x})$ directly. The importance of the near-field signature comes from the fact that it can be calculated from the *far-field signature of a point far away*. This is seen by comparison of Eq. (79), Eq. (80), and Eq. (81) which yields the following relation between near- and far-field signatures

$$N_c(\hat{\mathbf{s}}) = M_{L,\hat{\mathbf{s}}}(\mathbf{c}-\mathbf{a}) F_a(\hat{\mathbf{s}}). \quad (82)$$

This is the pivotal equation of the FMM. It allows the translation of the far-field information gained from triangles near point \mathbf{a} to near-field information to triangles near point \mathbf{c} .

A. The Single-level FMM

For numerical evaluation of the integrals the signatures are defined on properly chosen collocation points \hat{s}_q on the unit sphere and thus, translation of a signature from \mathbf{a} to \mathbf{c} means translation of all of the values $F_a(\hat{s}_q)$.

In order to set up a FMM, the geometry is covered with a set of cubes. For each cube the far-field signature for the \hat{s}_q is calculated at the cube center from the triangles inside. Using Eq. (82) this far-field signature is then translated to the near-field signatures defined at the center of the other cubes. Once the far-field contributions have been collected inside some cube, the sum $A(\mathbf{x})$ can be evaluated by integration of the near-field signature over the unit sphere for any point inside the cube.

Because one needs well separated cells for the application of Eq. (82) the far-field contributions of a cube are not collected from immediate neighbors of a cube. The cube and its immediate neighbors are called the near-field of the cube, and the contributions of all triangles in this near-field are calculated like in the classical BEM. The FMM described so far is the single-level FMM, which reduces the cost of a matrix-vector product from $O(N^2)$ to $O(N^{3/2})$ [15].

B. The Multilevel FMM

A further speed-up of the matrix-vector product can be achieved using a multilevel FMM [16]. There, the far-field signatures are collected for larger and larger groups of cubes and the expensive translations to the near-field signatures using Eq. (82) can be reduced. In a practical implementation of the algorithm, the cubes are sorted into an octree and the signatures are collected in the center of the parent cubes from their eight childs. This multilevel FMM is based on the fact that the signatures can be shifted to different centers. Setting $\mathbf{a} - \mathbf{y}_{jm} = (\mathbf{a} - \mathbf{b}) + (\mathbf{b} - \mathbf{y}_{jm})$ in Eq. (80) gives

$$F_a(\hat{s}) = e^{ik\hat{s} \cdot (\mathbf{a}-\mathbf{b})} F_b(\hat{s}) \quad (83)$$

and setting $\mathbf{x} - \mathbf{c} = (\mathbf{x} - \mathbf{d}) + (\mathbf{d} - \mathbf{c})$ in Eq. (81) gives

$$N_d(\hat{s}) = e^{ik\hat{s} \cdot (\mathbf{d}-\mathbf{c})} N_c(\hat{s}) \quad (84)$$

Thus, shifting of a signature is done by a simple multiplication with an exponential function of imaginary argument. Now it is important that moving up the octree, the distances $|\mathbf{a} - \mathbf{b}|$ between the cube centers become larger and larger and by multiplication with the exponential function the spectral content of the signatures increases. Thus, representing the signatures on the larger cubes needs more and more collocation points on the unit sphere^e Using the collocation points of the largest cube for all smaller ones would rapidly blow-up memory consumption and thus an interpolation procedure is necessary between the signatures of different levels of the tree. Since interpolation has to be done for a lot of levels for large problems, a sufficiently accurate interpolation procedure must be provided.

In the DLR FMM code a method based on special surface-harmonic expansions on the sphere has been implemented. This expansion was proposed by S.Orszag for the solution of partial differential equations on the sphere [23] and is briefly summarized here. Orszag observed that the general form of a truncated surface-spherical harmonic expansion of a function $F(\varphi, \vartheta)$ on the sphere is

$$F(\varphi, \vartheta) = \sum_{m=-M}^M b_m(\vartheta) e^{im\varphi}, \quad b_m(\vartheta) = \sin^{|m|} \vartheta f_m(\cos \vartheta) \quad (85)$$

where $f_m(x)$ is a polynomial of grade $M - |m|$. φ is the longitude coordinate on the sphere and ϑ the co-latitude coordinate. Since the exponent $|m|$ of the sine-function couples φ and ϑ closely, no fast transform methods are available. Arguing that the rapid decrease of b_m with increasing m near the poles $\vartheta = 0, \pi$ is only of minor interest in numerical simulations, Orszag proposes the simplification

$$b_m(\vartheta) = \begin{cases} f_m(\cos \vartheta) & , m \text{ even} \\ \sin \vartheta f_m(\cos \vartheta) & , m \text{ odd} \end{cases} \quad (86)$$

Now, $\sin \vartheta$ can be extracted from the sum over m and the φ - and ϑ -directions are largely decoupled. A fast transformation can be used using FFTs in φ -direction and matrix-vector products in ϑ -direction.

^e Moving up the tree, more and more information is collected in the signatures and it is obvious that more values are needed to represent it.

In the DLR FMM code the interpolation was implemented as follows. In order to facilitate the integration over the sphere the usual equidistant points in φ - and Gauss-Legendre points in ϑ -direction are chosen as collocation points on the sphere [20]

$$\varphi_j = \frac{\pi}{q}j, \quad j = 0, 1, \dots, 2q-1, \quad \text{and } \pi \geq \vartheta_l \geq 0, \quad l = 0, 1, \dots, q+1 \quad (87)$$

The $\vartheta_l, l = 1, 2, \dots, q$ are calculated from the collocation points $-1 < x_l < 1$ of the Gauss-Legendre integration using $\vartheta_l = \arccos x_l$. The ansatz for a function on the unit sphere then reads

$$F(\varphi, \vartheta) = \sum_{m=-q+1}^{q-1} e^{im\varphi} b_m(\vartheta), \quad b_m(\vartheta) = \begin{cases} \sum_{k=0}^{q+1} a_{mk} P_k(\cos \vartheta) & , m \text{ even} \\ \sum_{k=1}^q a_{mk} \sin \vartheta P_k(\cos \vartheta) & , m \text{ odd} \end{cases} \quad (88)$$

where $P_k(x)$ are Legendre polynomials. Defining the vectors

$$\mathbf{a}_m = a_{mk}, \quad \mathbf{b}_m = b_m(\vartheta_l), \quad (89)$$

and the matrices

$$\mathbf{C} = C_{kl} = P_k(\cos \vartheta_l), \quad \mathbf{S} = S_{kl} = \sin \vartheta_l P_k(\cos \vartheta_l), \quad (90)$$

one can write at the collocation points

$$F_{jl} = F(\varphi_j, \vartheta_l) = \sum_{m=-q+1}^{q-1} e^{im\varphi_j} b_m \quad (91)$$

$$\mathbf{b}_m = \begin{cases} \mathbf{C} \mathbf{a}_m & , m \text{ even} \\ \mathbf{S} \mathbf{a}_m & , m \text{ odd} \end{cases}. \quad (92)$$

Given function values F_{jl} at the collocation points, the \mathbf{b}_m can be obtained by FFTs and the expansion coefficients by $\mathbf{a}_m = \mathbf{C}^{-1} \mathbf{b}_m$ for even m and by $\mathbf{a}_m = \mathbf{S}^{-1} \mathbf{b}_m$ for odd m . For one interpolation on a level only the $(q+2) \times (q+2)$ matrix \mathbf{C} and the $q \times q$ -matrix \mathbf{S} must be stored. The resolution q depends on the cut-off value L of the transfer function, Eq. (78). It has been found that choosing q about 20% larger than L is sufficiently accurate for integration and interpolation on the sphere.

The multilevel FMM allows the reduction of the complexity of a matrix-vector product from $O(N^2)$ to $O(N \log N)$. Fig. 13 shows the scaling in the range $10^3 \lesssim N \lesssim 10^7$ for monopole scattering at a sphere. The graphs for linear, $N^{3/2}$, and quadratic scaling are shown for comparison.

VIII. Rig 145 – Shielding Calculations

In order to demonstrate the applicability of the CROR model, a noise shielding calculation of a Rig 145 CROR installed at an 1/6th-scale modified DLR-F6 aircraft geometry (F6OR) using the DLR FMM code has been performed. It should be emphasized however that the Rig 145 CROR model is constructed from CFD data of the uninstalled case, i.e., no inflow disturbances from pylon and airframe are taken into account.

The surface of the F6OR geometry is discretized with about 212000 triangles resulting in a surface resolution of about 9 elements per wavelength. The CROR is located at the right side of the aft fuselage near the vertical tailplane (cf. Fig. 14b). Fig. 14 depicts the 6 dipole rings of the front (blue) and rear (red) rotor as well as the modulus of the surface pressure on the F6OR. The calculated mode was $(m_0, m_1) = (1, 3)$. Fig. 15 shows the unshielded and shielded pressure in a plane below the geometry. The CROR position is near the center of the plane and the nose of the aircraft points to the left. One sees a noise amplification on the side of the CROR, created mainly by reflection of sound at the horizontal tailplane.

IX. Summary and Conclusions

A frequency domain model for the loading noise of a CROR with different rotational speeds has been developed which can be used for BEM/FMM shielding calculations. The model has been checked using a time domain calculation with rotating dipoles.

The comparison of the CROR model prediction with experimental data validates the method for predictions of the blade passing frequencies of the two rotors and the first interaction tones in the rotor plane and the directivity is also validated for the front rotor BPF tone. The observed errors in this range are less than 3 dB. The CROR model

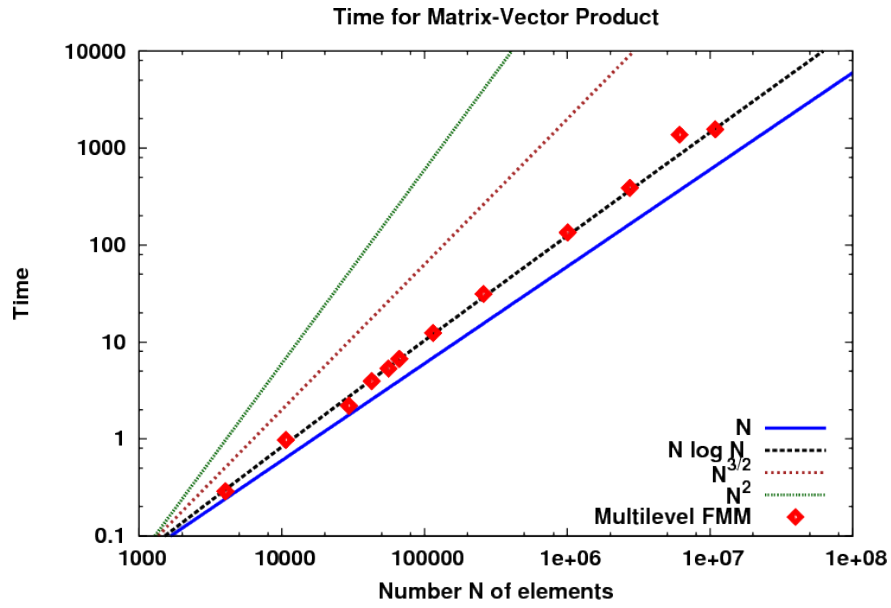


Figure 13. $N \log N$ scaling of the matrix-vector product in the range $10^3 \lesssim N \lesssim 10^7$ for monopole scattering at a sphere using the DLR FMM code.

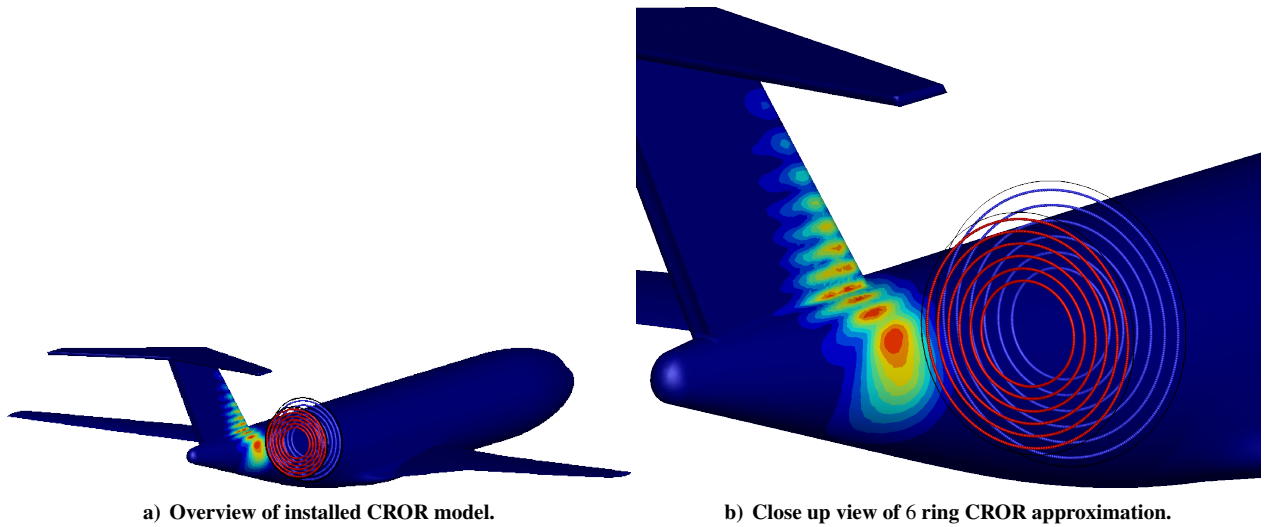


Figure 14. 1/6th-scale F6OR geometry with Rig 145 dipole rings and modulus of surface pressure. Mode $m_0 = 1, m_1 = 3$

in general provides higher SPL values for the BPF and for the summation tones when compared with the measured data. It is assumed, that the overprediction of the high frequency tones is due to turbulence interaction of the tones with the wind tunnel shear layers in the experiment. Another possible cause is the simplification of assuming straight rotor blades, which requires further investigation.

The applicability of the model has been demonstrated using the DLR FMM code for shielding calculations of a CROR installed at a modified DLR F6 aircraft geometry.

X. Acknowledgements

Funding for the current project was provided by the German Ministry of Economy through the project OPERO. The authors want to acknowledge Tony Parry from RR plc. for the fruitful discussions and the input to the paper.

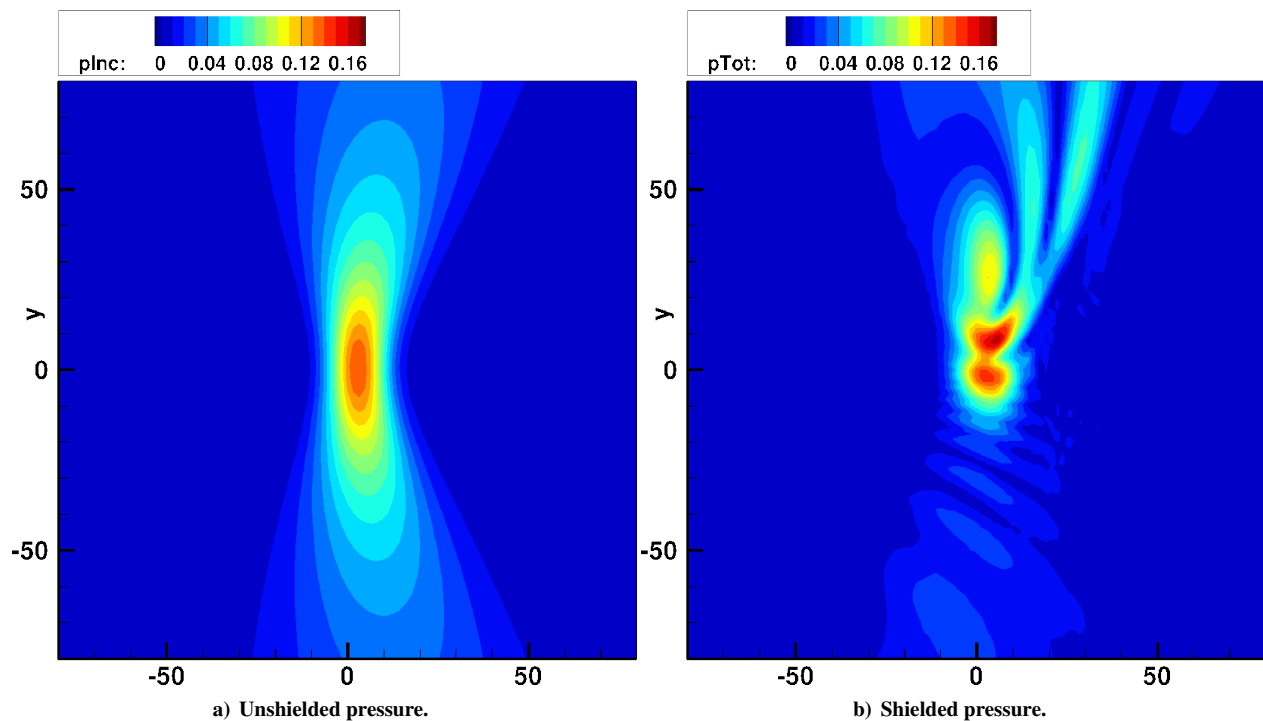


Figure 15. Modulus of pressure in plane below 1/6th-scale F6OR geometry. CROR position near center, nose of aircraft points to the left.

References

- [1] Burton, A. J. and Miller, G. F., "The Application of Integral Equation Methods to the Numerical Solution of some Exterior Boundary Value Problems," *Proceedings of the Royal Society, London*, Vol. A 323, 1971, pp. 201–210.
- [2] Glegg, S. A. L., "Effect of Centerbody Scattering on Propeller Noise," *AIAA Journal*, Vol. 29, No. 4, 1991, pp. 572–576.
- [3] Müller, L., *Quellformulierung für Fernfeldschallberechnung mit einem Schallstrahlenverfahren bei installierten gegenläufigen Propellern*, Diplomarbeit, Technische Universität Braunschweig, Oktober 2009.
- [4] Vaníček, P., "Approximate spectral analysis by least-squares fit," *Astrophysics and Space Science*, Vol. 4, No. 4, 1969, pp. 387–391.
- [5] Vaníček, P., "Further development and properties of the spectral analysis by least-squares," *Astrophysics and Space Science*, Vol. 12, 1971, pp. 10–33.
- [6] Akkermans, R. A. D., Delfs, J. W., Lummer, M., Siefert, M., Caruelle, B., and Tiedemann, C., "Handling of Non-Periodic Contra Rotating Open Rotor Data," *18th AIAA/CEAS Aeroacoustics Conference, Colorado Springs, CO, USA*, No. 2012-2262, 2012.
- [7] Ricouard, J., Julliard, E., Omais, M., Regnier, V., Parry, A., and Baralon, S., "Installation effects on contra-rotating open rotor noise," *16th AIAA/CEAS Aeroacoustics Conference, Stockholm, Sweden*, No. 2010-3795, 2010.
- [8] Márquez Gutiérrez, C. O., Stürmer, A., Clemen, C., and Grimminger, A., "Validation of Actuator Disk Simulations of CROR Propulsion Systems at Low-Speed Flight Conditions," *30th AIAA Applied Aerodynamics Conference*, No. 2012-2787, June 2012.
- [9] Márquez Gutiérrez, C. O., "Private communication."
- [10] Morse, P. M. and Ingard, K. U., *Theoretical Acoustics*, McGraw-Hill Book Company, Inc., New York/Toronto/London, 1968.
- [11] Amini, S., "On the choice of the coupling parameter in boundary integral formulations of the exterior acoustic problem," *Applicable analysis*, Vol. 35, No. 1, 1990, pp. 75–92.
- [12] Kleinman, R. and Kress, R., "On the condition number of integral equations in acoustics using modified fundamental solutions," *IMA Journal of applied mathematics*, Vol. 31, No. 1, 1983, pp. 79.
- [13] Laursen, M. E. and Gellert, M., "Some Criteria For Numerically Integrated Matrices and Quadrature Formulas for Triangles," *International Journal for Numerical Methods in Engineering*, Vol. 12, 1978, pp. 67–76.
- [14] Kirkup, S. M., "BEMHELM: BEM for Helmholtz Problems," <http://www.boundary-element-method.com/helmholtz/manual/index.htm>, 1998.

- [15] Coifman, R., Rokhlin, V., and Wandzura, S., "The Fast Multipole Method for the Wave Equation: A Pedestrian Prescription," *IEEE Antennas and Propagation Magazine*, Vol. 35, No. 3, June 1993, pp. 7–12.
- [16] Rokhlin, V., "Diagonal Forms of Translation Operators for the Helmholtz Equation in Three Dimensions," Research Report YALEU/DCS/RR-894, Yale University, Department of Computer Science, March 25 1992.
- [17] Rokhlin, V., "Diagonal Forms of Translation Operators for the Helmholtz Equation in Three Dimensions," *Applied and Computational Harmonic Analysis*, Vol. 1, 1993, pp. 82–93.
- [18] Rahola, J., "Diagonal Forms of the Translation Operators in the Fast Multipole Algorithm for Scattering Problems," *BIT Numerical Mathematics*, Vol. 36, No. 2, June 1996, pp. 333–358.
- [19] Darve, E., "The Fast Multipole Method I: Error Analysis and Asymptotic Complexity," *SIAM Journal on Numerical Analysis*, Vol. 38, No. 1, 2000, pp. 98–128.
- [20] Darve, E., "The Fast Multipole Method: Numerical Implementation," *Journal of Computational Physics*, Vol. 160, 2000, pp. 195–240.
- [21] Sylvand, G., "Performance of a parallel implementation of the FMM for electromagnetics applications," *International Journal for Numerical Methods in Fluids*, Vol. 43, No. 8, 2003, pp. 865–879.
- [22] Carayol, Q. and Collino, F., "Error Estimates in the Fast Multipole Method for Scattering Problems Part 2: Truncation of the Gegenbauer Series," *ESAIM: Mathematical Modelling and Numerical Analysis*, Vol. 39, No. 1, 2005, pp. 183–221.
- [23] Orszag, S. A., "Fourier Series on Spheres," *Monthly Weather Review*, Vol. 102, January 1974, pp. 56–75.